

ACOUSTIC DETERMINATION OF THE CRITICAL POINT OF METHANE
UTILIZING A VARIABLE VOLUME SPHERICAL RESONATOR
UNDER ISOTHERMAL CONDITIONS

By

D. C. RENTZ

A DISSERTATION PRESENTED TO THE GRADUATE SCHOOL
OF THE UNIVERSITY OF FLORIDA IN PARTIAL FULFILLMENT
OF THE REQUIREMENTS FOR THE DEGREE OF
DOCTOR OF PHILOSOPHY

UNIVERSITY OF FLORIDA

1994

Copyright 1994

by

D. C. Rentz

To Ashley, who believed I could do anything.

ACKNOWLEDGEMENTS

It is impossible to acknowledge all the people who have helped in the production of this work. However, there are several teachers who have been instrumental in propelling me to the completion of my graduate studies. There is my wife, Ashley Rentz, who has taught me of the matters of the heart. My parents, Ray and Marilyn Rentz, who have taught me how to live among others. My friends, Patti and Pierre Robitaille, who have always been the example of how I would wish to treat others. My mentor, Dr. Samuel Colgate, who has taught me how to work within my craft. There are others, but these stand out above the rest. To those mentioned and those that have gone unsung, I say thank you.

TABLE OF CONTENTS

ACKNOWLEDGEMENTS	iv
LIST OF TABLES	vii
LIST OF FIGURES	viii
ABSTRACT	xi
CHAPTER 1	
INTRODUCTION	1
Motivation for Examining the Critical Point of Methane	1
CHAPTER 2	
HISTORICAL OVERVIEW	5
First Thoughts	5
Background	5
Critical point location from isotherm studies	7
Critical point location from isochore studies	8
Critical point location from isobar studies	11
The Speed of Sound as a Probe for the Critical Point	12
CHAPTER 3	
THEORY	16
Wave Mechanics	16
Acoustics	21
Acoustic Spectrum Analysis	26
CHAPTER 4	
EXPERIMENTAL	30
Procedure	30
Initial Gas Loading	33
Attainment of System Critical Density	36
Data Acquisition	38
Calibration	40
Heise Pressure Gauge Calibration	40
System RTD Temperature Calibration	42
Apparatus Detail	47
Resonator	47

Transducers	48
System RTD Placement	51
Bellows Construction Detail	51
CHAPTER 5	
RESULTS	57
Spherical Resonator	57
Acoustic Spectra	58
Data Manipulation	63
Curve Fitting	76
Critical pressure	76
Critical temperature	80
Thermodynamic Surface	82
CHAPTER 6	
DISCUSSION	84
The Critical Point of Methane	84
Gas Impurity	86
System RTD	86
Heise Pressure Gauge	88
Precision of Technique	89
Personal Note	91
REFERENCE LIST	95
BIOGRAPHICAL SKETCH	100

LIST OF TABLES

Table 3-1. $\xi_{l,m}$, eigenvalues for spherical Bessel function of order m.	25
Table 4-1. Instrumentation Summary.	54
Table 4-1. (continued)	55
Table 4-1. (continued)	56
Table 5-1. System dependent variables for equation fitted to experimental data.	80
Table 6-1. Methane critical point parameters found in the literature.	85

LIST OF FIGURES

Figure 2-1. Typical P , \tilde{V} and T surface construct and associated two dimensional plots.	6
Figure 2-2. Pressure-volume isotherms of carbon dioxide in the critical region.	8
Figure 2-3. Pressure-temperature isochores of benzene in the critical region.	10
Figure 2-4. Determination of the critical point for hydrogen from measurements of the liquid density ρ_l and gaseous density ρ_g	12
Figure 3-1. Acoustic spectrum of methane from a spherical cavity, (three inch radius).	27
Figure 3-2. Typical detail of individual gas resonance frequencies, (excerpts from fig. 3-1).	28
Figure 4-1. Experimental apparatus schematic.	31
Figure 4-2. Control instrumentation schematic.	32
Figure 4-3. Calibration plot for the Heise gauge vs. ADC units.	42
Figure 4-4. Pressure calibration setup.	43
Figure 4-5. Response of system RTD and precalibrated RTD under identical conditions.	44
Figure 4-6. Plot of System RTD vs. Precalibrated RTD exhibiting strong linear response at low temperatures.	45
Figure 4-7. Triple point of water calibration for the precalibrated RTD.	46
Figure 4-8. Spherical resonator schematic.	47
Figure 4-9. Construction detail for transducer mount.	50

Figure 4-10. Construction detail of system temperature shroud.	52
Figure 4-11. Construction detail of bellows assembly.	53
Figure 5-1. Typical acoustic spectrum recorded well away from the critical point.	59
Figure 5-2. Typical acoustic spectrum recorded near the critical point.	60
Figure 5-3. Excerpt from an acoustic spectrum near the critical point.	61
Figure 5-4. Excerpt from an acoustic spectrum after time and volume has changed, (frequencies are shifted toward zero frequency).	61
Figure 5-5. Superposition of two acoustic spectra excerpts illustrating the rapid change in resonant frequency and amplitude that accompanies a small change in volume near the critical point.	63
Figure 5-6. Typical relationship between system speed of sound and system volume near the critical temperature.	64
Figure 5-7. Typical relationship between the system speed of sound and the system density.	65
Figure 5-8. Typical relationship between the system speed of sound and the system pressure.	67
Figure 5-9. Plot of all data sets of pressure and speed of sound on a common set of axes.	69
Figure 5-10. Largest temperature variation for a single data run.	71
Figure 5-11. Pressure dependence on temperature for data run that deviates most from isothermal conditions.	73
Figure 5-12. Frequency dependence on temperature for data set that deviates most from isothermal conditions.	73
Figure 5-13. Plot of all data runs of system speed of sound vs. system temperature on a single set of axes.	74

Figure 5-14. Three dimensional plot of system variables; pressure, temperature and speed of sound.	75
Figure 5-15. Plot of system speed of sound versus system pressure with fitted equation overlaid. . .	79
Figure 5-16. Plot of system temperature versus system pressure corresponding to minimum values for system speed of sound for each data run.	81
Figure 5-17. Thermodynamic surface of the critical point of methane.	83
Figure 6-1. Sub critical pressure data taken near the critical density.	89
Figure 6-2. Above critical pressure data taken near the critical density.	90
Figure 6-3. Sound velocity at selected temperatures as a function of pressure.	91
Figure 6-4. Graph of sound velocity as a function of pressure containing all twenty data runs from this experiment.	92

Abstract of Dissertation Presented to the Graduate School
of the University of Florida in Partial Fulfillment of the
Requirements for the Degree of Doctor of Philosophy

ACOUSTIC DETERMINATION OF THE CRITICAL POINT OF METHANE
UTILIZING A VARIABLE VOLUME SPHERICAL RESONATOR UNDER
ISOTHERMAL CONDITIONS

By

D. C. Rentz

April, 1994

Chairperson: Samuel O. Colgate
Major Department: Chemistry

A novel apparatus for the study of thermodynamic properties of fluids has been fabricated and utilized to examine the critical point of methane. A spherical acoustic resonator assembly with a variable volume was used as a sensitive probe for examining the thermodynamic surface of methane in its critical region. The resonator was built to operate over broad ranges of pressure and temperature, (0-4000psi and 77-525K). A unique stainless steel bellows arrangement was incorporated to allow a variable system volume which for the first time permitted acoustic phase mapping under isothermal conditions. The frequency of the third radially symmetric normal mode of vibration was measured and related to the sonic speed of methane within the spherical cavity. The critical values for pressure and temperature were

measured and reported as $4.6081 \pm 0.0015 \text{ MPa}$ and $189.695 \pm 0.021 \text{ K}$ respectively. A plot of system pressure, temperature and sonic speed was constructed to delineate the thermodynamic surface of the critical region of methane.

CHAPTER 1 INTRODUCTION

Motivation for Examining the Critical Point of Methane

Methane is the principal component of natural gas. As such, it is used extensively as a fuel for many different processes. The demand for this natural resource has established methane as a commodity of great economic as well as political importance.¹ As a result of this demand, methane has been made available on an increasing scale throughout the twentieth century. This availability and importance have made methane an attractive material for scientific study. Consequently, a wealth of summarized data can be found in the scientific literature.

The ready availability of numerous tabulations of data for methane has made it appealing for theoretical work on a unified equation of state. An equation of state is the mathematical model of a system that relates pressure, temperature and specific volume or density in an analytical way. The history of efforts to establish reliable equations of state is rich dating back to the work of Boyle as early as 1661. Since that time, many refinements have been introduced and many equations of state have been proposed.²

No general equation of state, however, has yet proven to be analytic at all practical values of pressure, temperature and density. This has not been particularly detrimental as equations exist which are in reasonable agreement with experiment under limited conditions that are not too far toward the extremes of any of the three variables. Since the great majority of scientific activity involves matter in states which are removed from outermost conditions, major efforts toward achieving a more unified equation of state slowed to a crawl for many years.³

Recent developments in chemistry, physics and astronomy have involved studies of matter under conditions well beyond those addressed by established equations of state. Those temperatures and pressures exhibited by laser induced plasmas and observable celestial bodies were not accessible at the time when traditional equations of state were being formulated. Consequently, new equations applicable over broader ranges are needed, and activity in generating such equations is growing.

The critical region has proven especially difficult to characterize analytically because it exhibits unusually large fluctuations in the local density. Typically, a gas is much less dense than its corresponding liquid. In the critical region, however, the properties of the gas and liquid states become indistinguishable. As a consequence, microscopic droplets of liquid tend to evaporate while simultaneously

vapor molecules tend to aggregate in small clusters. Some thermodynamic relationships become discontinuous at the critical point. The ability to describe such behavior is very difficult mathematically.

The most fruitful treatment of discontinuities associated with the critical region utilizes scaling laws to link thermodynamic behavior on either side of the critical point. Thermodynamic properties on one side of the critical point are dealt with as almost separate entities from the same properties on the other side. Because of this drastic change in thermodynamic behavior, it has become common practice to base equation of state formulations as beginning at the critical point. Thermodynamic detail is then viewed in terms of its distance from the critical point.

Mathematically, extensive use is made of reduced variables such as^{4,5}

$$T_{\text{red}} = \left(\frac{T - T_c}{T_c} \right), \quad P_{\text{red}} = \left(\frac{P - P_c}{P_c} \right), \quad \text{and} \quad \rho_{\text{red}} = \left(\frac{\rho - \rho_c}{\rho_c} \right)$$

where T is the temperature, P is the pressure, ρ is the density and the symbols with the subscript c represent the same variables at the critical point. It is apparent that for any theoretical model based on this approach to be successful, it is vital that the parameters for the critical point be undisputed.

Recently, however, a paper was published that questions the latest P , T and ρ values for the critical point of

methane.⁶ Such a question calls for a reexamination of the critical point parameters for methane.

CHAPTER 2 HISTORICAL OVERVIEW

First Thoughts

In order to put the current work in proper context, it is important to be acquainted with past efforts to examine the critical region and identify the critical point. The relative merits and drawbacks of each method must be evaluated in order to illustrate the novelty and utility of the work presented here. Ideally, the current work should represent an advance in experimental technique and yield results of high precision and accuracy. Final judgement as to the extent the current work achieves these goals is left to the reader, but it is the burden of the author to try to illustrate how they were pursued and what has been accomplished.

Background

For a single component system the critical point is typically identified on some type of phase diagram. The pressure, molar volume and temperature relationship can be represented by a three dimensional construct. The surface shown in figure 2-1 is a typical portion of a P , \tilde{V} , T relationship. The line depicted by ABCDE is the coexistence line between liquid and vapor states. Point C corresponds to

the highest temperature on the coexistence line and is defined as the critical point.⁷

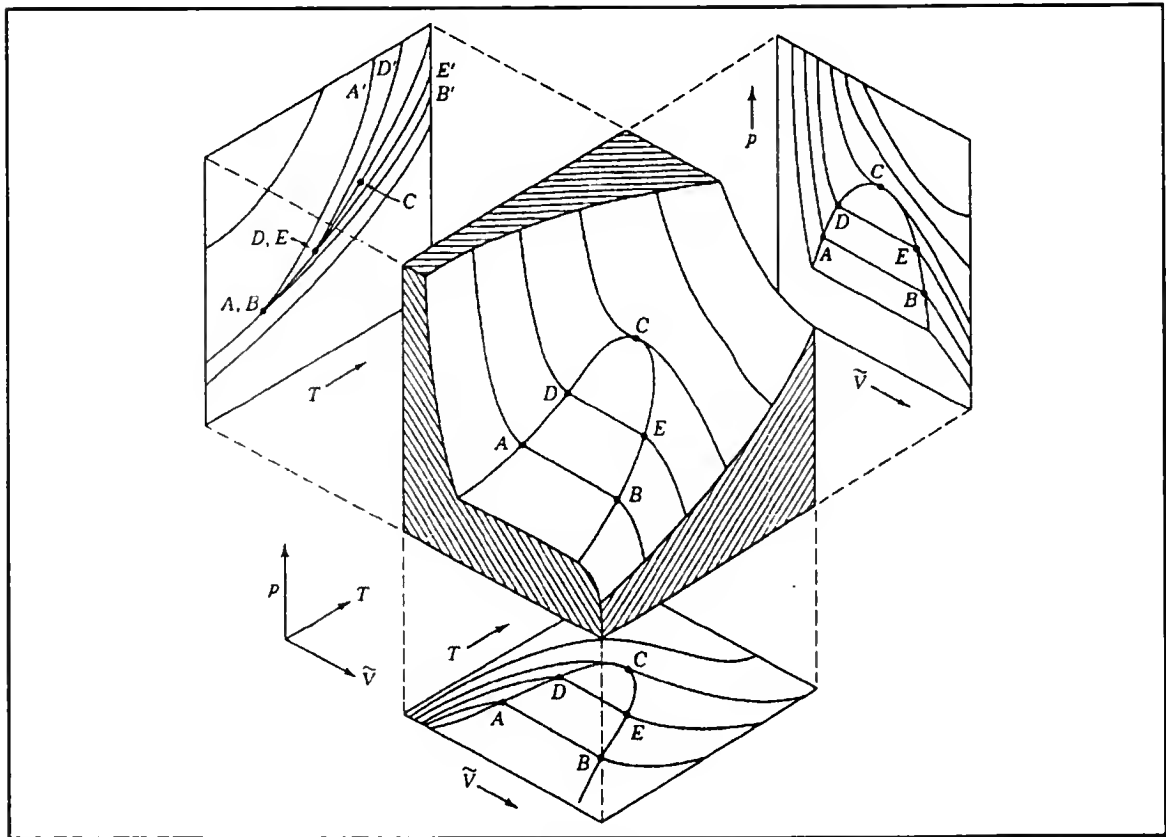


Figure 2-1. Typical P , \tilde{V} and T surface construct and associated two dimensional plots.

The three dimensional construct in figure 2-1 is cumbersome and difficult to visualize. Each of the three projections in figure 2-1 represents a simpler view of the thermodynamic surface. The upper left view shows P versus T plotted for various values of constant volume. Each line represents data for a unique constant volume and is termed an isochore. The upper right view shows P versus \tilde{V} data plotted while maintaining constant temperature. Each line represents

data taken at a unique constant temperature and is termed an isotherm. Similarly, the lower center view is T and \tilde{V} data plotted while maintaining constant pressure. Each line represents data taken at a different constant pressure and is termed an isobar. Any of the three projections has sufficient information to reconstruct the three dimensional surface.

Several established methods for determining the location of the critical point exist. Traditional methods correspond to production of one of the three projections mentioned above. A short discussion of each is illustrative of the difficulties faced by the experimentalist and yields insight into the problems that must be addressed to achieve an accurate measurement of the critical point.

Critical point location from isotherm studies

This method requires the temperature to be held constant while the molar volume (or the density) is slowly varied. A series of pressure vs. volume plots for CO_2 is reproduced in figure 2-2. As the molar volume is varied, the pressure change becomes depressed and eventually reaches a stationary value as the critical point is approached and surpassed.⁸ The slope of the isotherm, $(\partial P / \partial \tilde{V})_T$, approaches and becomes zero at and below the critical point.

The method works well, especially for systems with T_c near room temperature, but suffers from an inability to determine the critical point with high precision. Well above

the critical point it is quite apparent that the slope of the line never reaches zero over a range of volumes. Likewise, well below the critical point it is apparent that the slope of the line is zero over a range of volumes. However, near the critical point, it becomes a subjective matter to determine at what values of the state variables the slope of the line first becomes zero and not just merely close to zero.

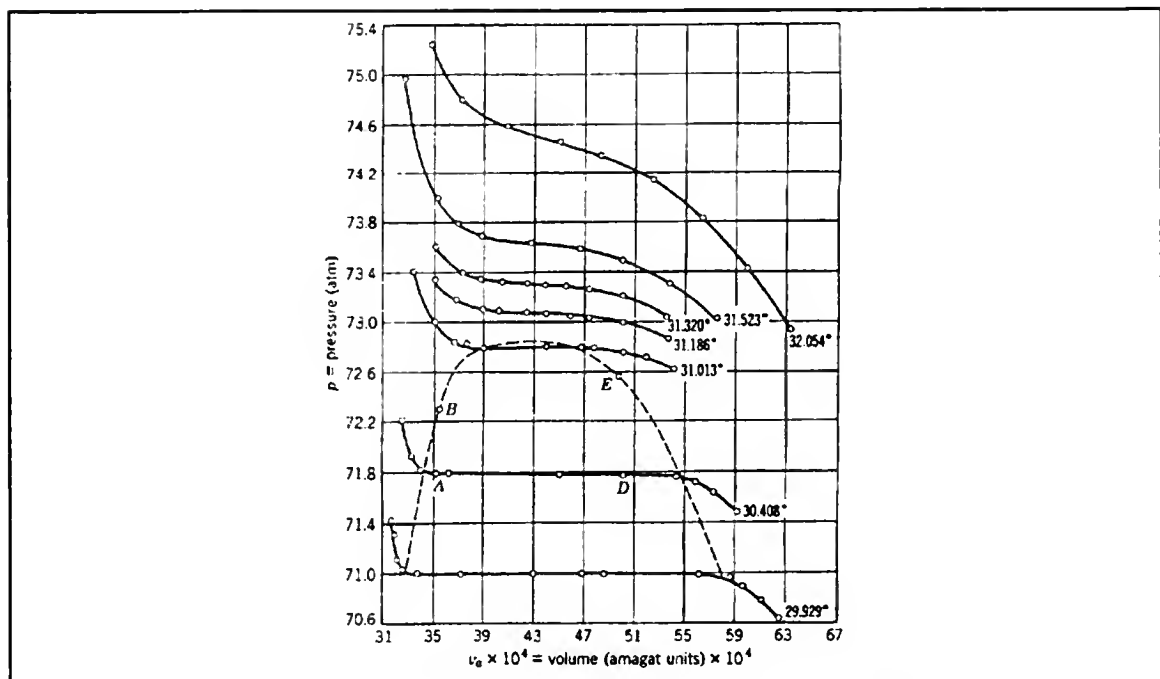


Figure 2-2. Pressure-volume isotherms of carbon dioxide in the critical region.

Critical point location from isochore studies

Two major methods exist for determining the critical point from isochore studies. The first examines the deviation of the isochore curve. A constant volume, high pressure bomb

is loaded with a predetermined density of a material under study. The temperature is varied and the pressure measured. A plot of pressure vs. temperature is constructed. If the average density within the containment vessel is lower than the critical density, then a downward deflection is observed in the graphed data. The onset of the deflection occurs at the corresponding dew point. Conversely, if the average density within the containment vessel is higher than the critical density, then an upward deflection is observed in the graphed data precisely at the corresponding bubble point. Only when the average density is equal to the critical density does no deflection occur. Figure 2-3 illustrates typical results of this method for benzene.⁹

This technique is straightforward to perform, but precision and accuracy are poor. Substantial change in density is required for even a modest break or discontinuity in the plot. Even the use of curve fitting and differentiation techniques still fails to yield high precision.

The second method dealing with isochores is equivalent to the first, but takes advantage of a peculiarity that occurs at the critical point, namely, the disappearance of the liquid/gas separator, the meniscus.¹⁰ At the critical point, the properties of the liquid and gas become indistinguishable. Consequently, the difference in density necessary to produce a visible separator no longer exists and the meniscus simply

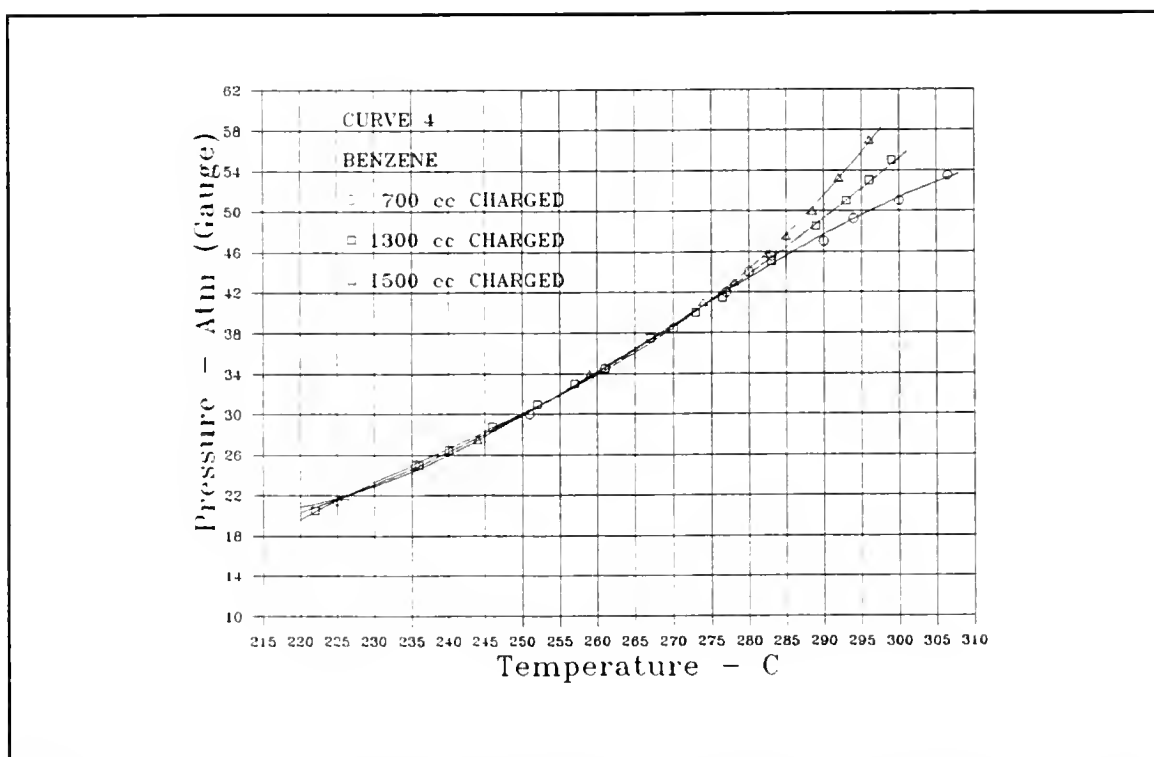


Figure 2-3. Pressure-temperature isochores of benzene in the critical region.

disappears in the middle of a containment vessel of uniform horizontal cross section. If the average density of the system is less than the critical density, the meniscus will appear to fall slowly and eventually the vessel will be filled with gas. If on the other hand, the average system density is greater than the critical density, the meniscus will slowly rise and eventually the vessel will be filled with liquid. The temperature, pressure and density at which the meniscus disappears precisely halfway up the vessel are taken as the critical parameters.

This technique is quite sensitive as it is easy to tell if the meniscus is moving up, down or is stationary. Near the

critical point, however, the difference between the thermodynamic properties of the liquid and gas becomes minute. Therefore, the meniscus becomes more difficult to observe. As a result, the reported values of the critical point parameters eventually become dependant on the subjective judgement of the experimentalist.

Critical point location from isobar studies

This technique is known as the method of rectilinear diameter and is illustrated in figure 2-4.^{11,12} It requires plotting of the densities, (related to the molar volume), of the liquid and saturated vapor gas over a wide range of temperatures extending as close as possible to the critical point. The average of the two densities is calculated and also plotted on the same graph.

The average density and the temperature are fitted to an equation of form $\frac{1}{2}(\rho_g + \rho_l) = \rho_0 + \alpha T$. The analytical line is extended until it intersects the coexistence curve. The values obtained from the intersection are taken as the critical point parameters.

The density of the gas and liquid change very rapidly near the critical point and defining the shape of the density curves becomes very difficult. Also, the line representing the average density has some curvature and a linear fit is questionable. These two ambiguities make it difficult to make

more than a reasonable estimate of the critical point parameters by this method.

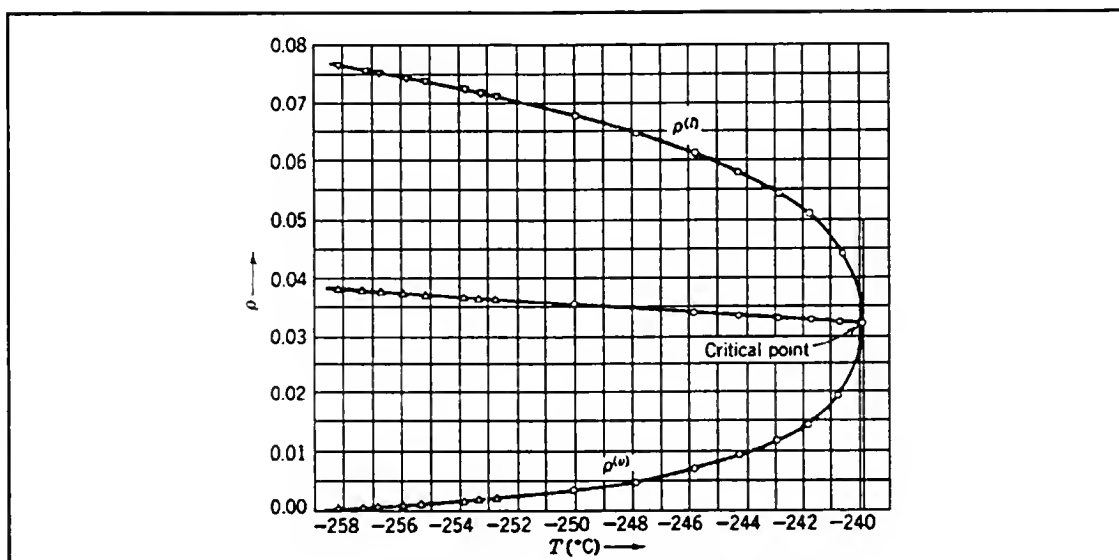


Figure 2-4. Determination of the critical point for hydrogen from measurements of the liquid density ρ_l and gaseous density ρ_g .

The Speed of Sound as a Probe for the Critical Point

Each of the above mentioned techniques for probing the critical point requires a certain amount of subjectivity. Considering the measurement of isotherms, for example, the ability to distinguish between line slopes almost equal to zero and actually equal to zero is typically subject to experimental error greater than the limits of uncertainty with which the critical point parameters are desired to be known.

What is needed then is a technique that takes advantage of the very liability which normally limits the desired

accuracy. Examination of the projection in figure 2-1 corresponding to the isotherms in the $P-\tilde{V}$ plane shows the critical isotherm passes through point C where the isotherm slope first becomes equal to zero. A function which depends on the slope of the critical isotherm can have a very rapidly changing value at point C. The slope of such a function will be dependent on $(\partial P^2/\partial \tilde{V}^2)_T$ and will also be zero at the critical point. Consequently, if such a function exists, it would have a rapidly changing slope that goes to zero at the critical point instead of a very slowly changing slope as seen in the critical isotherm in figure 2-1. This type of behavior may be more readily identifiable experimentally than deciding when a virtually flat line actually becomes completely flat.

Thermodynamics explores the many relationships between state variables.¹³ These include the density, the enthalpy, the free energy and others. Heat capacity is such a variable. One equation that relates the heat capacity of the system at constant volume to other state variables is

$$\tilde{C}_v = T \left(\frac{\partial \tilde{V}}{\partial T} \right)_S \left(\frac{\partial \tilde{V}}{\partial T} \right)_P \left(\frac{\partial P}{\partial \tilde{V}} \right)_T$$

Where \tilde{C}_v is the molar heat capacity
 S is the system entropy

Since $(\partial P / \partial \tilde{V})_T$ approaches and becomes zero at the critical point, while the other terms have nonzero finite values, the heat capacity at the critical state also becomes zero. A three-dimensional plot of this state function against temperature and molar volume would be observed as a spike depression that extends asymptotically towards zero from a relatively gently curved surface. This type of behavior is very well suited for locating the critical point of a thermodynamic system, as a spike depression is much more readily observable than the change in slope of an almost flat line.^{14,15}

Unfortunately, accurately measuring the heat capacity for a system is an arduous task. What is needed now is a property with similar behavior but one which is easily measured. Such a state function is the propagation speed of a pressure wave through the system or the speed of sound. A thermodynamic equation for the speed of sound is¹⁶

$$c_0^2 = -\tilde{V}^2 \frac{\gamma}{M} \left(\frac{\partial P}{\partial \tilde{V}} \right)_T \quad \text{Eqn. 2-1}$$

In this equation, γ is the ratio of the heat capacity at constant pressure to the heat capacity at constant volume and M is the Molecular weight of the species under study. The variable c_0 is the thermodynamic speed of sound at zero frequency. We see that the speed of sound for a system also depends on a term that becomes zero at the critical point. It

should be a very sensitive probe for the critical point. Several methods are known for measurement of the sonic speed. The method employed in this work is extremely sensitive. It involves measurement of standing acoustic wave frequencies of cavity bound systems.

Virtually any type of containment vessel for the thermodynamic fluid may be used as long as the geometry is well characterized and the wave equation is solvable for the allowed cavity resonant frequencies. Often a cylindrical resonator has been utilized with the sound generator and the sound receiver located at opposite ends of the cylinder.¹⁷ However, propagation of sound through a cylinder is subject to a bothersome perturbation due to viscous drag on the cylinder walls which complicates the final analysis. A more satisfactory technique is the utilization of a spherical resonator that accommodates some purely radial modes of vibration. Such vibrations correspond to a sound wave emanating from the center of the sphere and travelling outward symmetrically to the chamber walls and rebounding back toward the center. These radial modes are free from viscous effects which arise when sound waves have components of motion laterally along vessel walls. A more detailed look at the theory of spherical acoustic resonators and their use is found in the next chapter.

CHAPTER 3 THEORY

Wave Mechanics

The transmission of a wave through a fluid medium is governed by the general wave equation¹⁸

$$\nabla^2 \Psi = \frac{1}{c^2} \frac{\partial^2 \Psi}{\partial t^2} \quad \text{Eqn. 3-1}$$

Where ∇^2 is the Laplacian, Ψ is the wave function, t is time and c is the wave velocity. The Laplacian in spherical coordinates is¹⁹

$$\nabla^2 = \frac{1}{r^2} \frac{\partial}{\partial r} r^2 \frac{\partial}{\partial r} + \frac{1}{r^2 \sin \theta} \frac{\partial}{\partial \theta} \sin \theta \frac{\partial}{\partial \theta} + \frac{1}{r^2 \sin^2 \theta} \frac{\partial^2}{\partial \phi^2}$$

If the wave equation is assumed to be for a standing wave, that is for a wave whose amplitude does not depend on time, then it is possible to assume a separable wave function such that

$$\Psi = \psi e^{-i\omega t} \quad \text{Eqn. 3-2}$$

Where $i^2 = -1$, $\omega = 2\pi\nu$, ν = frequency.

Substitution of eqn. 3-2 into eqn. 3-1 yields

$$\nabla^2 \psi = \frac{-\omega^2}{c^2} \psi \quad \text{Eqn. 3-3}$$

Further, if it is assumed that the wave function is separable in each of the spherical coordinates, then the equation for the spatial wave function can be written as

$$\psi = R(r) \Theta(\theta) \Phi(\phi) \quad \text{Eqn. 3-4}$$

Substitution of eqn. 3-4 into eqn. 3-3 and utilizing the Laplacian yields

$$\begin{aligned} & \frac{1}{R(r)} \frac{1}{r^2} \frac{d}{dr} r^2 \frac{dR(r)}{dr} + \frac{\omega^2}{c^2} + \\ & \frac{1}{\Theta(\theta)} \frac{1}{r^2} \frac{1}{\sin\theta} \frac{d}{d\theta} \sin\theta \frac{d\Theta(\theta)}{d\theta} + \\ & \frac{1}{\Phi(\phi)} \frac{1}{r^2 \sin^2\theta} \frac{d^2\Phi(\phi)}{d\phi^2} = 0 \end{aligned} \quad \text{Eqn. 3-5}$$

The task of finding the wave function that satisfies eqn. 3-5 is daunting in appearance. However, it is possible to separate eqn. 3-5 into three factors each of which deals with only one of the three spherical coordinates. Once this is accomplished, each factor is separately set to zero and the resulting one dimensional differential equations are solved subject to reasonable boundary conditions. The three equations to be solved are

$$\frac{d}{dr} r^2 \frac{dR(r)}{dr} + \left(\frac{\omega^2}{c^2} r^2 - A \right) R(r) = 0 \quad \text{Eqn. 3-6}$$

$$\sin\theta \frac{d}{d\theta} \sin\theta \frac{d\Theta(\theta)}{d\theta} + (A \sin^2\theta - B) \Theta(\theta) = 0 \quad \text{Eqn. 3-7}$$

$$\frac{d^2\Phi(\phi)}{d\phi^2} + B\Phi(\phi) = 0 \quad \text{Eqn. 3-8}$$

Where 'A' and 'B' are separation constants.

Equation 3-8 represents the axial angle contribution to the overall wave function and is the easiest to solve. If we allow the separation constant 'B' to equal n^2 , then the general solution would be

$$\Phi(\phi) = \sin(n\phi) \quad \text{or} \quad \cos(n\phi) \quad \text{Eqn. 3-9}$$

Since each of these functions is periodic, the boundary condition requires they be single valued as ϕ changes by any multiple of 2π . Therefore, the separation constant n is constrained to have an integral value. That is, $n = 0, \pm 1, \pm 2, \dots$

Substitution of n^2 for 'B' in eqn. 3-7 and rewriting yields

$$\sin\theta \frac{d}{d\theta} \sin\theta \frac{d\Theta(\theta)}{d\theta} + (A \sin^2\theta - n^2) \Theta(\theta) = 0$$

Since the separation constant 'n' is squared, no new information is gained by considering its negative integer values. Making the change of variable, $\eta = \cos \phi$, yields the following

$$(1-\eta^2) \frac{d^2\Theta(\eta)}{d\eta^2} - 2\eta \frac{d\Theta(\eta)}{d\eta} + \left[A - \frac{n^2}{1-\eta^2} \right] \Theta(\eta) = 0 \quad \text{Eqn. 3-10}$$

Eqn. 3-10 is recognizable as a Legendre function, provided the separation constant 'A' is set equal to $m(m+1)$ and m is constrained to be an integer equal to or greater than zero. The notation of the Legendre function is written as $P_m^n(\eta)$ because the solution of the differential equation is assumed to be a polynomial. The general solution for eqn. 3-10 is

$$\Theta(\eta) = P_m^n(\eta) = (1-\eta^2)^{n/2} \frac{d^n}{d\eta^n} P_m(\eta) \quad \text{Eqn. 3-11}$$

where $P_m(\eta)$ is the associated Legendre polynomial derived from the following recursion formulas

For $m = 0, 2, 4, \dots$

$$P_m(\eta) = a_0 \left[1 + \frac{(-m)(1+m)}{2!} \eta^2 + \frac{(-m)(2-m)(1+m)(3+m)}{4!} \eta^4 + \dots \right. \\ \left. + \frac{(-m)(2-m)(4-m) \dots (2s-2-m)(1+m)(3+m) \dots (2s-1+m)}{2s!} \eta^{2s} + \dots \right]$$

For $m = 1, 3, 5, \dots$

$$P_m(\eta) = a_1 \eta \left[1 + \frac{(1-m)(2+m)}{3!} \eta^2 + \frac{(1-m)(3-m)(2+m)(4+m)}{5!} \eta^4 + \dots \right. \\ \left. + \frac{(1-m)(3-m) \dots (2s-1-m)(2+m)(4+m) \dots (2s+m)}{(2s+1)!} \eta^{2s} + \dots \right]$$

The value chosen for 'm' is also equal to the highest value for the power of the independent variable found in the Legendre polynomial obtained from the above recursion formulas. Consequently, if 'm' is chosen such that 'm' is less than 'n', then

$$\frac{\partial^n}{\partial \eta^n} P_m(\eta) = 0$$

From this, it follows that the general solution stated in eqn. 3-11 has the additional constraint that $0 < n \leq m$.

The combination of eqn. 3-9 and 3-11 yields the solution of the angular portion of the overall wave equation. Traditionally, this combination of functions has been termed the spherical harmonics, $Y_{m,n}(\eta, \phi)$, and takes the form

$$Y_{m,n}(\eta, \phi) = \Theta(\eta) \Phi(\phi) \\ = (1-\eta^2)^{\frac{n}{2}} \frac{d^n}{d\eta^n} P_m(\eta) \frac{\cos}{\sin}(n\phi) \quad \text{Eqn. 3-12}$$

Substituting 'A' = m(m+1) into eqn. 3-6 yields

$$\frac{d}{dr} r^2 \frac{dR(r)}{dr} + (k^2 r^2 - m(m+1)) R(r) = 0$$

$$\text{Where } k = \frac{\omega}{c}$$

Expanding the derivative and making the change of variable $\zeta = kr$ leads to

$$\frac{d^2 R(\zeta)}{d\zeta^2} + \frac{2}{\zeta} \frac{dR(\zeta)}{d\zeta} + [\zeta^2 - m(m+1)] \frac{R(\zeta)}{\zeta^2} = 0 \quad \text{Eqn. 3-13}$$

This equation has a general solution for $R(\zeta)$ known as the spherical Hankel function of order m, $h_m(\zeta)$.²⁰

$$R_m(\zeta) = h_m(\zeta) = \frac{i^{-m}}{i\zeta} \sum_{s=0}^m \frac{(m+s)!}{s!(m-s)!} \left(\frac{i}{2\zeta} \right)^s e^{i\zeta} \quad \text{Eqn. 3-14}$$

The combination of eqns. 3-2, 3-12 and 3-14 gives the overall solution for the wave function defined in eqn. 3-1

$$\begin{aligned} \Psi &= R_m(\zeta) Y_{m,n}(\eta, \phi) e^{-i\omega t} \\ \Psi &= \frac{i^{-m}}{i\zeta} \sum_{s=0}^m \frac{(m+s)!}{s!(m-s)!} \left(\frac{i}{2\zeta} \right)^s e^{i\zeta} \cdot \\ &\quad (1-\eta^2)^{\frac{n}{2}} \frac{d^n}{d\eta^n} P_m(\eta) \cos(n\phi) e^{-i\omega t} \end{aligned} \quad \text{Eqn. 3-15}$$

Acoustics

Often, it is not necessary to utilize the entire solution to the wave equation to interpret acoustic experiments in a spherical resonator. The purely radial wave functions are

most easily related to thermodynamic variables. Two constraints on the wave function provide the bridge between theory and practicality.

The first constraint is that the sound introduced inside a spherical cavity is allowed to propagate throughout the cavity. The spherical Hankel function, eqn. 3-14, can be separated into two portions; a real part and an imaginary part as follows

$$h_m(\zeta) = j_m(\zeta) + in_m(\zeta)$$

The real part of this separated function, $j_m(\zeta)$, is known as a spherical Bessel function of order m while the imaginary part, $n_m(\zeta)$, is known as a spherical Neuman function of order m . For example, the first two spherical Hankel functions corresponding to $m=0$ and $m=1$ are

$$R_0(\zeta) = \frac{e^{i\zeta}}{i\zeta}$$

$$R_1(\zeta) = \frac{-e^{i\zeta}}{\zeta} - i \frac{e^{i\zeta}}{\zeta^2}$$

substituting the identity $e^{i\zeta} = \cos(\zeta) + i\sin(\zeta)$ and rearranging yields

$$\begin{aligned} R_0(\zeta) &= h_0(\zeta) = j_0(\zeta) + in_0(\zeta) \\ &= -\frac{\sin(\zeta)}{\zeta} - i \frac{\cos(\zeta)}{\zeta} \end{aligned}$$

Eqn. 3-16

$$\begin{aligned}
R_1(\zeta) &= h_1(\zeta) = j_1(\zeta) + in_1(\zeta) \\
&= \left(\frac{\sin(\zeta)}{\zeta^2} - \frac{\cos(\zeta)}{\zeta} \right) + i \left(\frac{-\sin(\zeta)}{\zeta} - \frac{\cos(\zeta)}{\zeta^2} \right)
\end{aligned}$$

Eqn. 3-17

While either the real part, $j_m(\zeta)$, or the imaginary part, $n_m(\zeta)$, are solutions for the radial contribution to the wave equation, only the real part also has the property of having a finite value when $r \rightarrow 0$. Therefore, $R_m(\zeta)$ can be simplified to just $j_m(\zeta)$ for standing waves inside an enclosed chamber. Once the first two spherical Bessel functions are known, all subsequent functions for $j_m(\zeta)$ can be derived from the recursion formula

$$j_{m+1}(\zeta) = \frac{1}{\zeta} (2m+1)j_m(\zeta) - j_{(m-1)}(\zeta)$$

The second constraint is that as the acoustic wave meets the wall of the chamber it must cease its forward motion. Writing this constraint in mathematical terms leads to

$$\left(\frac{dR_m(\zeta)}{dr} \right)_{r=a} = \left(\frac{dj_m(\zeta)}{dr} \right)_{r=a}^{\text{inside resonator}} = 0 \quad \text{Eqn. 3-18}$$

where a is the radius of the spherical cavity. Applying this constraint to the real part of eqn. 3-16 and eqn. 3-17 leaves

$$\left(\frac{dj_0(\zeta)}{dr} \right)_{r=a}^{\text{inside resonator}} = \tan(\zeta) - \zeta = 0 \quad \text{Eqn. 3-19}$$

$$\left(\frac{dj_1(\zeta)}{dr} \right)_{r=a}^{\text{inside resonator}} = \frac{\sin(\zeta)}{\zeta} + \frac{2\cos(\zeta)}{\zeta^2} - \frac{2\sin(\zeta)}{\zeta^3} = 0 \quad \text{Eqn. 3-20}$$

There are an infinite number of solutions or eigenvalues that satisfy either of eqns. 3-19 or 3-20. Separate eigenvalues are designated by the general symbol $\xi_{l,m}$, where l represents where in the infinite series of solutions a particular solution falls. In an analogous manner to naming the more familiar hydrogen atomic orbitals, $\xi_{1,0}$ is termed the 1s eigenvalue, $\xi_{2,3}$ is termed the 2f eigenvalue and so forth.

The lowest twenty-three eigenvalues were calculated by Lord Rayleigh in 1872²¹ and H. G. Ferris extended the list to include the lowest eighty-four eigenvalues.²² The list is recreated in table 3-1.

Each eigenvalue represents a distinct normal mode of acoustic vibration of an elastic fluid constrained by a rigid spherical wall. Drawing discussion results together leads to

$$\xi_{l,m} = \zeta = kr_{r=a} = \frac{\omega a}{c} = \frac{2\pi a}{c} \nu \quad \text{Eqn. 3-21}$$

Equation 3-21 ties together the theoretical solution of the wave equation ($\xi_{l,m}$) and the real world experiment ($a, \nu_{l,m}$). The eigenvalues are well known and the resonator radius and sound frequencies can be accurately measured.

Table 3-1. $\xi_{\ell,m}$, eigenvalues for spherical Bessel function of order m .

$\xi_{\ell,m}$	ℓ	m	Name	$\xi_{\ell,m}$	ℓ	m	Name
2.08158	1	1	1p	17.4079	1	15	1t
3.34209	1	2	1d	17.9473	4	5	4h
4.49341	1	0	1s	18.1276	2	11	2n
4.51408	1	3	1f	18.3565	3	8	3k
5.64670	1	4	1g	18.4527	1	16	1u
5.94036	2	1	2p	18.4682	5	3	5f
6.75643	1	5	1h	18.7428	6	1	6p
7.28990	2	2	2d	19.2628	4	6	4i
7.72523	2	0	2s	19.2704	2	12	2o
7.85107	1	6	1i	19.4964	1	17	1v
8.58367	2	3	2f	19.5819	3	9	3l
8.93489	1	7	1j	19.8625	5	4	5g
9.20586	3	1	3p	20.2219	6	2	6d
9.84043	2	4	2g	20.3714	6	0	6s
10.0102	1	8	1k	20.4065	2	13	2q
10.6140	3	2	3d	20.5379	1	18	1w
10.9042	3	0	3s	20.5596	4	7	4j
11.0703	2	5	2h	20.7960	3	10	3m
11.0791	1	9	1l	21.2312	5	5	5h
11.9729	3	3	3f	21.5372	2	14	2r
12.1428	1	10	1m	21.5779	1	19	1x
12.2794	2	6	2i	21.6667	6	3	6f
12.4046	4	1	4p	21.8401	4	8	4k
13.2024	1	11	1n	21.8997	7	1	7p
13.2956	3	4	3g	22.0000	3	11	3n
13.4721	2	7	2j	22.5781	5	6	5i
13.8463	4	2	4d	22.6165	1	20	1y
14.0663	4	0	4s	22.6625	2	15	2t
14.2580	1	12	1o	23.0829	6	4	6g
14.5906	3	5	3h	23.1067	4	9	4l
14.6513	2	8	2k	23.1950	3	12	3o
15.2446	4	3	4f	23.3906	7	2	7d
15.3108	1	13	1q	23.5194	7	0	7s
15.5793	5	1	5p	23.6534	1	21	1z
15.8193	2	9	2l	23.7832	2	16	2u
15.8633	3	6	3i	23.9069	5	7	5j
16.3604	1	14	1r	24.3608	4	10	4m
16.6094	4	4	4g	24.3824	3	13	3q
16.9776	2	10	2m	24.4749	6	5	6h
17.0431	5	2	5d	24.6899	1	22	1a
17.1176	3	7	3j	24.8503	7	3	7f
17.2207	5	0	5s	24.8995	2	17	2v

Acoustic Spectrum Analysis

An acoustic resonance spectrum will typically show a series of frequencies that represent resonances allowed by eqn. 3-21. However, the acoustic spectrum may also contain other frequencies which are due to extraneous noise. Consequently, it is necessary to employ a stratagem for distinguishing the acoustic spectrum due to the sound propagating medium from all other features.

Assume that at any given moment for an isolated system, the speed of sound is a constant. Then, eqn. 3-21 taken for two different eigenvalues yields

$$\frac{\xi'}{\xi} = \frac{\frac{2\pi a}{c}}{\frac{2\pi a}{c}} \frac{v'}{v} \Rightarrow \frac{v}{\xi} = \frac{v'}{\xi'} \quad \text{Eqn. 3-22}$$

From equation 3-22, it can be seen that the ratio of $v_{t,m}/\xi_{t,m}$ should be a constant for resonances which involve only vibration of the contained fluid.

A typical acoustic spectrum is shown in figure 3-1. If a particular peak is thought to be a fluid resonance frequency, division by the correct eigenvalue followed by multiplication by subsequent eigenvalues should provide values for all other anticipated fluid resonance frequencies. If very few or no other peaks appear at the calculated locations, then either the assignment of the peak to a particular eigenvalue was wrong or the peak under scrutiny was not a

fluid normal mode. In such a fashion, the acoustic spectrum due to the fluid medium can always be 'singled out' from the background noise.

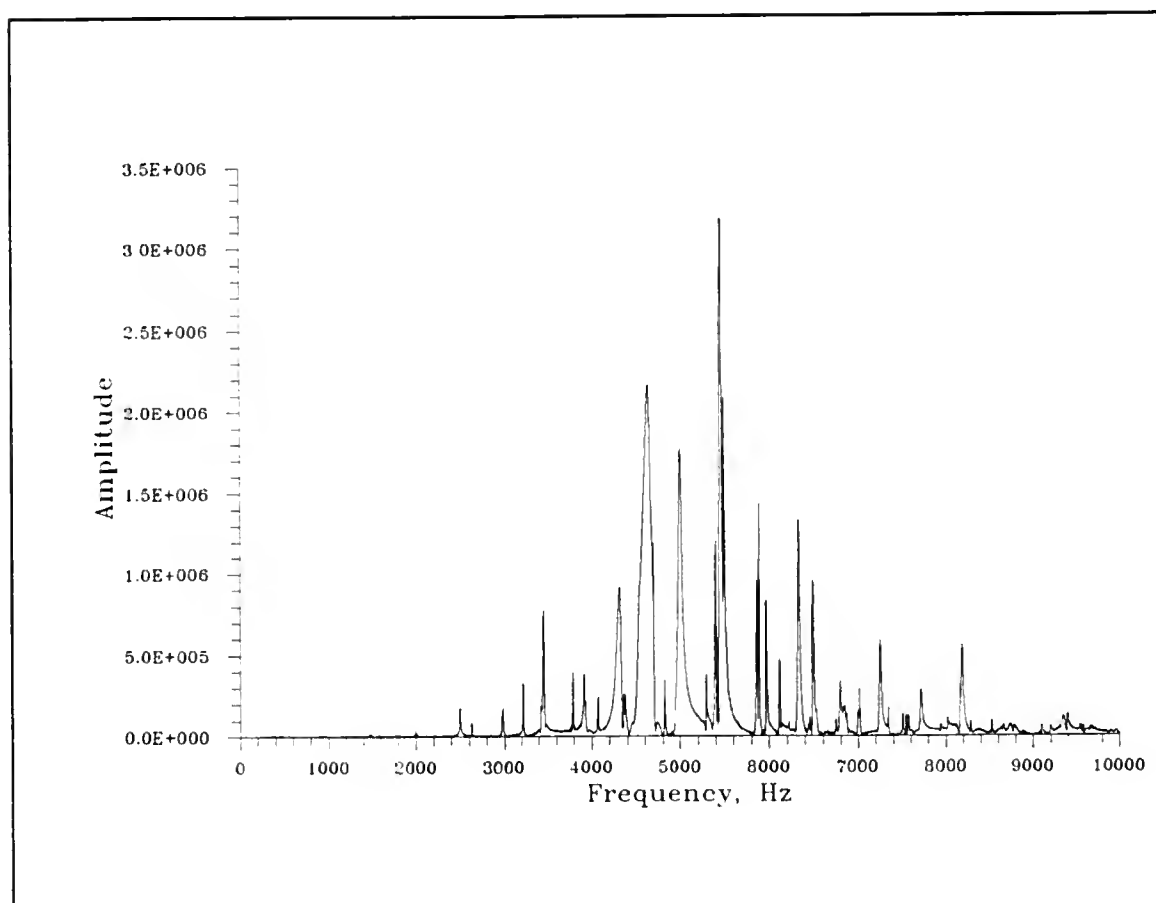


Figure 3-1. Acoustic spectrum of methane from a spherical cavity, (three inch radius).

Figure 3-2 shows typical gas resonance peaks in more detail. Peaks correspond to the 1g, 2p, 2d, and 3s resonances, respectively. Values for the ratio of $v/\xi_{l,m}$ for these same peaks are 442.22, 442.20, 442.10, and 442.36. Deviations in individual ratios are due to non-ideality in the spherical resonator. In a real apparatus, several factors can

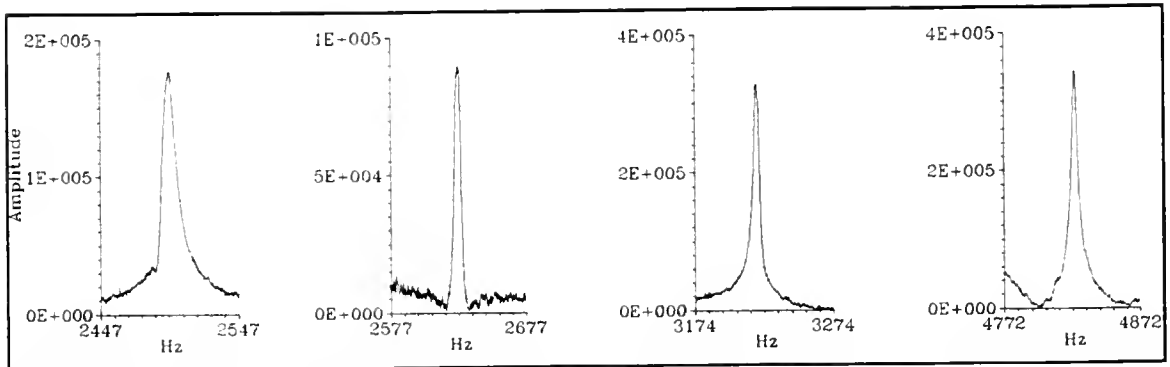


Figure 3-2. Typical detail of individual gas resonance frequencies, (excerpts from fig. 3-1).

perturb the observed frequencies. Mehl and Moldover^{23,24} have considered the most prominent of these and suggest that equation 3-21 should be expanded in the following manner

$$\nu = \frac{c}{2\pi a} \xi_{l,m} + \Delta\nu_s + \Delta\nu_{el} + \Delta\nu_t + \Delta\nu_{geom} + \dots$$

The added terms represent perturbations due to the thermal boundary layer effect at the resonator wall, the finite elastic compliance the resonator wall, the effects of filling tubulations connected to the resonator wall and deviations from perfect sphericity of the resonator wall. For a carefully designed and fabricated apparatus, these perturbations can be quite small. Corrections can be made either by theoretical treatments or by calibration.

The perturbations affect different modes of vibration differently. The purely radial modes are generally least perturbed and consequently one or more of the spherically symmetric resonances for which $m=0$ are often selected. Radial

modes involve no tangential motion of the fluid at the resonator walls and are not subject to the effects of viscous drag. Such resonances are generally very well defined and resolved from other allowed resonances. This facilitates easy identification and subsequent tracking.

CHAPTER 4 EXPERIMENTAL

Procedure

A spherical acoustic resonator assembly with a variable volume was utilized as a probe to locate the critical point of methane. Temperature, pressure and sonic speed were the primary variables that were tracked, but volume was also followed in a non analytical manner. None of the variables was measured directly, but each was followed as a more readily measurable related parameter. Figures 4-1 and 4-2 are schematic representations of the overall experiment. Figure 4-1 represents the physical apparatus while figure 4-2 represents the control instrumentation. For later reference, the tubulations, pump, resonator, inner bellows and RTD shroud are referred to as the sealed methane 'system'.

Several Sections of the apparatus have unique features that must be addressed separately to highlight construction detail. Calibrations of temperature and pressure measuring devices are included by necessity. Also, instrumentation and its accuracy are documented to illustrate the level of research that has been undertaken.

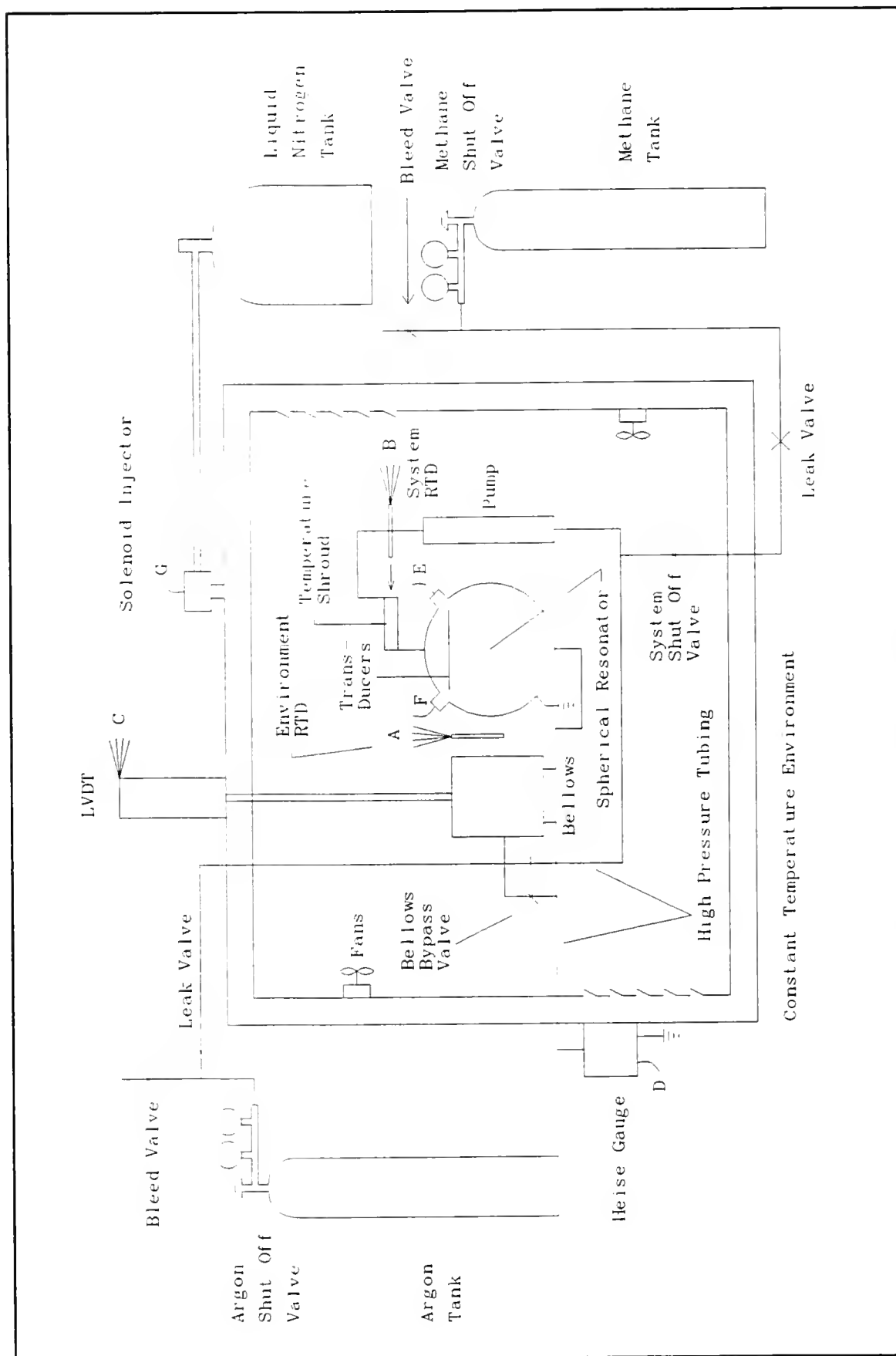


Figure 4-1. Experimental apparatus schematic.

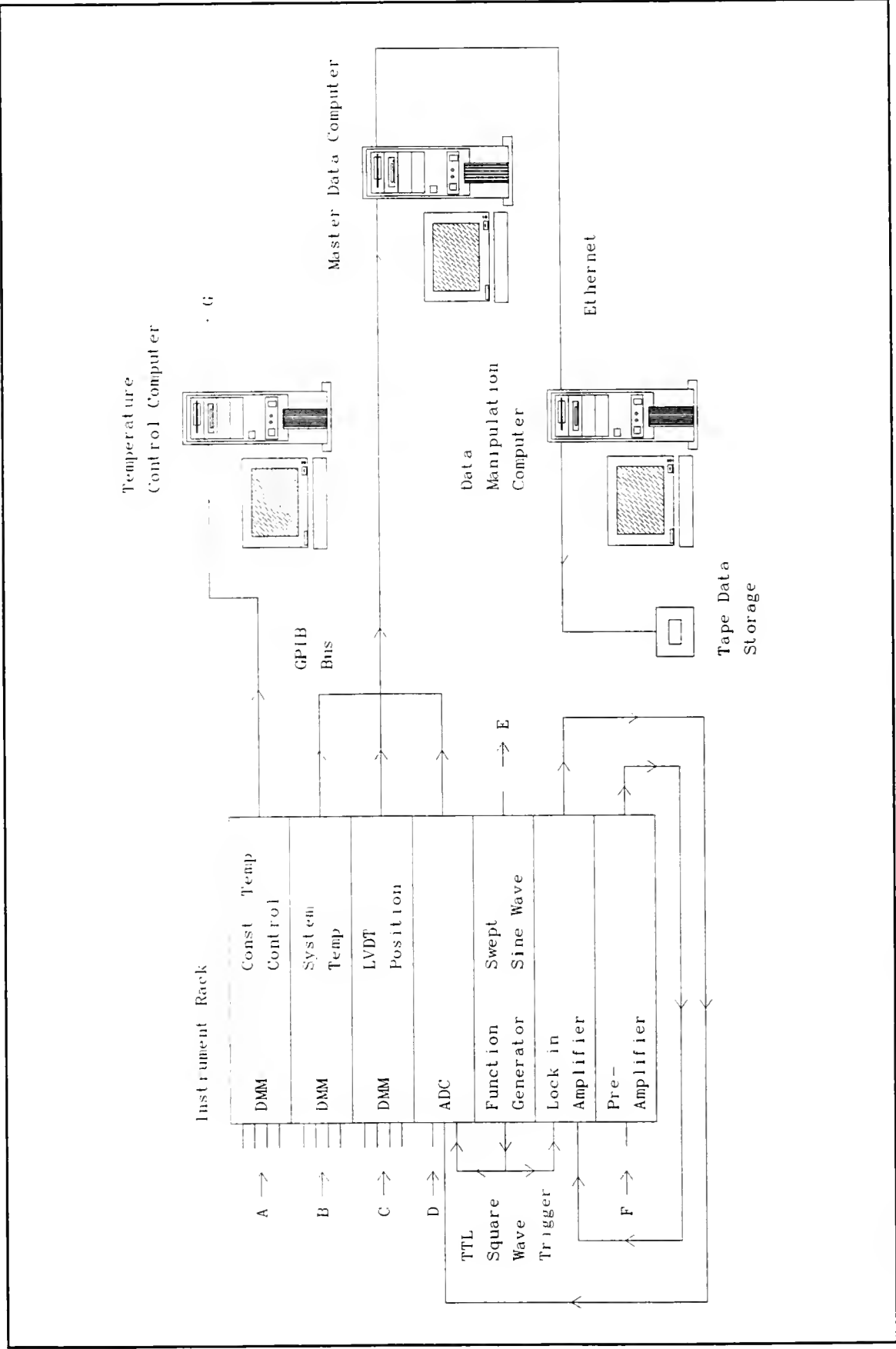


Figure 4-2. Control instrumentation schematic.

Initial Gas Loading

A brief overview of the experimental procedure allows a working insight into the technique. Research grade methane assayed at 99.99% pure from Scott Specialty Gas, Inc. was utilized as the experimental fluid. The entire system in contact with methane was of stainless steel construction to minimize the potential for chemical reaction with containment walls. To ensure initial methane purity within the system, a regimen of system purges was conducted in the following manner...

1. All valves were closed except for the bellows bypass valve, the system shut off valve and the methane shut off valve.
2. The mechanical vacuum pump was started.
3. The shut off valve to the mechanical vacuum pump was opened.
4. The entire system was evacuated for a period of several hours to ensure the system pressure fell below 10^{-3} torr.
5. The shut off valve to the mechanical vacuum pump was closed.
6. The leak valve to the methane tank was opened minutely to introduce methane slowly to the system.
7. System pressure was brought to about ten atmospheres as monitored by the Heise Gauge.

8. The leak valve to the methane tank was closed.
9. The system pump was started and allowed to run for about twenty minutes.
10. The entire procedure was repeated starting at step three for a total of six iterations.

The charging procedure required a period of approximately thirty hours. The bellows bypass valve was then closed for the duration of the experiment isolating one side of the bellows from the other. The liquid nitrogen tank was attached to the constant temperature environment and the system was cooled. The constant temperature environment RTD, (Resistance Temperature Device), was monitored until system temperature fell to near the anticipated critical value. Environment temperature was then kept constant to within ten millikelvin through the use of a computer control algorithm.

The methane leak valve and shut off valve were reopened minutely to bring the system pressure to a value as close as possible to the anticipated critical pressure. The argon leak valve and shut off valve were similarly opened so as to maintain comparable pressure on both sides of the fragile bellows. To prevent rupture of the bellows by excess pressure, bellows position was constantly monitored through the use of an LVDT, (Linear Variable Differential Transformer, a sensitive position transducer). The pressure difference across the bellows was not allowed to exceed a few pounds per square inch, (psi). Irreversible damage would have occurred

for $\Delta p \geq 70$ psi. In order to safeguard the system in the event of a dangerous pressure gradient, a copper rupture disc of lower strength was utilized.

Once system pressure was near the anticipated critical value, all valves except the system shut off valve, the argon shut off valve and the argon leak valve were closed. Argon gas continued to be introduced to the back side of the bellows in order to compress it slowly. On reaching the bellows minimum position, the argon shut off valve and the argon leak valve were closed and the argon bleed valve was opened to atmosphere. The system pump was put into operation to assure system homogeneity. Sufficient time was allowed for temperature equilibrium to be established. The argon leak valve was reopened to allow a slow bleed off of bellows back pressure. The movement of the bellows from minimum to maximum position provided a variable volume capability. Sweep time of the bellows full range of motion was typically slow at ten to twelve hours to ensure only small departures from equilibrium. During the volume sweep, the temperature was followed with the system RTD, the pressure was followed with the Heise digital Bourdon gauge and the acoustic spectrum was followed with the sonic transducers. All three instruments were serially polled and the results recorded periodically at one to two minute intervals under control of the master data computer.

Attainment of System Critical Density

Unfortunately, a proper system loading of methane could not be obtained simply by filling and cooling the system to the anticipated critical pressure and temperature and then sealing it off. Even a small error in attempting to match system pressure and temperature to critical values was greatly magnified out of proportion due to the pressure change approaching zero at the critical point. The purpose of this research was to use sonic speed as a sensitive detector of the critical state. The thermodynamic speed of sound approaches zero rapidly at the critical point where the pressure, temperature and density, (or molar volume), are at their critical values, (see chapter two). Subsequently, if the system density were below the critical value, each new value for the system speed of sound would increase as the bellows was swept outwards. Conversely, if the system density were above the critical density, each new value for the system speed of sound would decrease as the bellows was swept outwards. Only when the system density matched the critical density somewhere in the middle of the bellows sweep did the speed of sound first decrease, reach a minimum and finally increase.

The process for getting the system speed of sound to reach a minimum in the middle of the bellows sweep was quite laborious. In essence, the same procedure for taking a complete data acquisition run was repeated numerous times.

The bleed valve above the argon tank was opened to the atmosphere and the argon leak valve was opened sufficiently to allow the bellows to sweep from low to high volume over the course of ten to twelve hours. Temperature, pressure and an acoustic spectrum were taken about every two minutes. Only about thirty total data points were required to determine whether system density was high or low, so data acquisition was halted after about an hour. The bleed valve above the argon tank was then closed and the argon tank shut off valve was opened. Argon was fed to the back side of the bellows in order to recompress it. At that point, all argon valves were shut and the system was allowed sufficient time to resume a constant temperature. In the mean time, the raw data were transferred to the data manipulation computer where the acoustic signals could undergo fast Fourier transformation from the time domain into the frequency domain, (i.e., the acoustic resonance spectrum). Each acoustic spectrum was then viewed and its resonance peaks identified. Individual peaks were then tracked from one spectrum to the next.

Once the trend in the speed of sound was identified, the system density was adjusted accordingly by either adding methane to or bleeding methane from the system. The entire process was then repeated until the elusive minimum in the speed of sound was centered within the range of the variable volume of the bellows. Finally, the system shut off valve was closed in order to isolate the system from the surroundings.

Data Acquisition

The actual acquisition of data after loading the system to the proper density was largely uneventful. All of the procedures required for data acquisition had already been enabled. Initially, the bellows began stationary at its minimum position, the master data computer was brought to a monitoring state, and sufficient time was allowed for thermal equilibrium to be established throughout the system. The argon bleed valve was vented to atmosphere and the argon leak valve was adjusted to achieve a total bellows sweep time of ten to twelve hours.

When initial bellows movement passed a certain preset value just above its starting point, the monitoring master data computer switched to an active data acquisition state. The master data computer triggered the function generator to produce a sine wave with a frequency sweep from 0 to 10kHz over a period of about six seconds. The function generator also produced a synchronized TTL square wave that triggered the Analog to Digital Converter, (ADC), and the lock-in amplifier to begin data acquisition. The swept sine wave was utilized as an acoustic excitation source for the input sonic transducer. The acoustic signal was transmitted from one sonic transducer to the other by means of fluid vibration within the spherical resonator. The preamplifier increased the output sonic transducer signal and fed it to the lock-in amplifier. The lock-in amplifier controlled a frequency band

pass filter which allowed only the transmitted frequency that matched the excitation frequency to pass on to the ADC. The acoustic spectrum was converted from an analog to a digital signal by the ADC and recorded by the master data computer. Immediately afterward, the DMM (Digital Multi Meter) that tracked the system RTD, the DMM that tracked the LVDT, and the ADC that tracked the Heise gauge were serially polled and the results recorded by the master data computer. The master data computer then returned to its monitoring state and awaited the bellows movement to pass the next preset position that triggered the next iteration of the acquisition procedure.

In this way, data sets were acquired about every two minutes until the bellows movement reached a final value just below the bellows maximum position. The data acquisition program then self terminated and sounded an alarm to alert the operator that the bellows movement needed to be arrested. The argon bleed valve was closed and the argon shut off valve reopened long enough to recompress the bellows slowly to a minimum position. The temperature control program was adjusted to achieve a different working temperature and sufficient time was allowed for thermal equilibrium to reestablish. The entire procedure was reiterated at different temperatures to span the critical point parameters.

As the system temperature was settling back to a new constant value, the data recorded by the master data computer were transferred to the data manipulation computer. A

seventeen bit fast Fourier transform was performed on each raw acoustic signal. The acoustic data were transformed from the time domain to the frequency domain. Each spectrum was individually examined to identify acoustic resonance peaks. The individual peak frequencies were then tracked from one spectrum to the next in order to follow the system speed of sound. A data bank was constructed which contained the system speed of sound, the system pressure, the system temperature and the system volume. Finally, the entire data bank was saved on tape storage media for future reference. See table 4-1 at the end of this chapter for an instrumentation summary.

Calibration

Heise Pressure Gauge Calibration

In order to locate the critical pressure, it was essential to utilize an accurate pressure gauge. The Heise pressure gauge that was used in this experiment was calibrated just before and immediately after all the data sets were acquired. Since it was located in proximity to the cooled, constant temperature environment, the final calibration was performed with the constant temperature environment at the same temperature at which the experiment was run.

Calibration was performed by utilizing a dead weight pressure gauge. A cylinder with a freely sliding piston having tolerances which do not allow passage of fluid was an essential part of the calibration apparatus. Direct weight

was floated atop the piston and provided an absolute pressure, ($p=mg/\text{area}$, where m is the mass and g is the acceleration due to gravity), on the fluid within the calibration system. The weights were loaded under vacuum, so no correction for the pressure of the air was necessary.

The Heise gauge output was an analog voltage which was converted by the ADC to a digital format that could be acquired by the master data computer. The mass on the dead weight pressure gauge was compared to the ADC output and an equation was generated that converted ADC units directly into an absolute pressure measurement. The actual calibration plot is shown in figure 4-3.

The calibration plot for the Heise gauge was incapable of being extended to the pressure ranges involved in this experiment. Each of the weights used on the dead weight pressure gauge was certified by the manufacturer, but the calibration range extended only to 622 psia while experimental pressure ranges extended approximately fifty psi higher. However, the extreme linearity of the calibration line, (χ^2 squared for a linear regression fit of data was .99999952), lends confidence to extrapolation over this small range.

The experimental arrangement used for the pressure calibration is illustrated in figure 4-4. The high pressure pump was used to increase or decrease the pressure of the calibration system until the piston of the dead weight pressure gauge floated at midpoint of its length of travel.

The values given by the ADC and the masses/absolute pressures on the dead weight pressure gauge were used to generate figure 4-3.

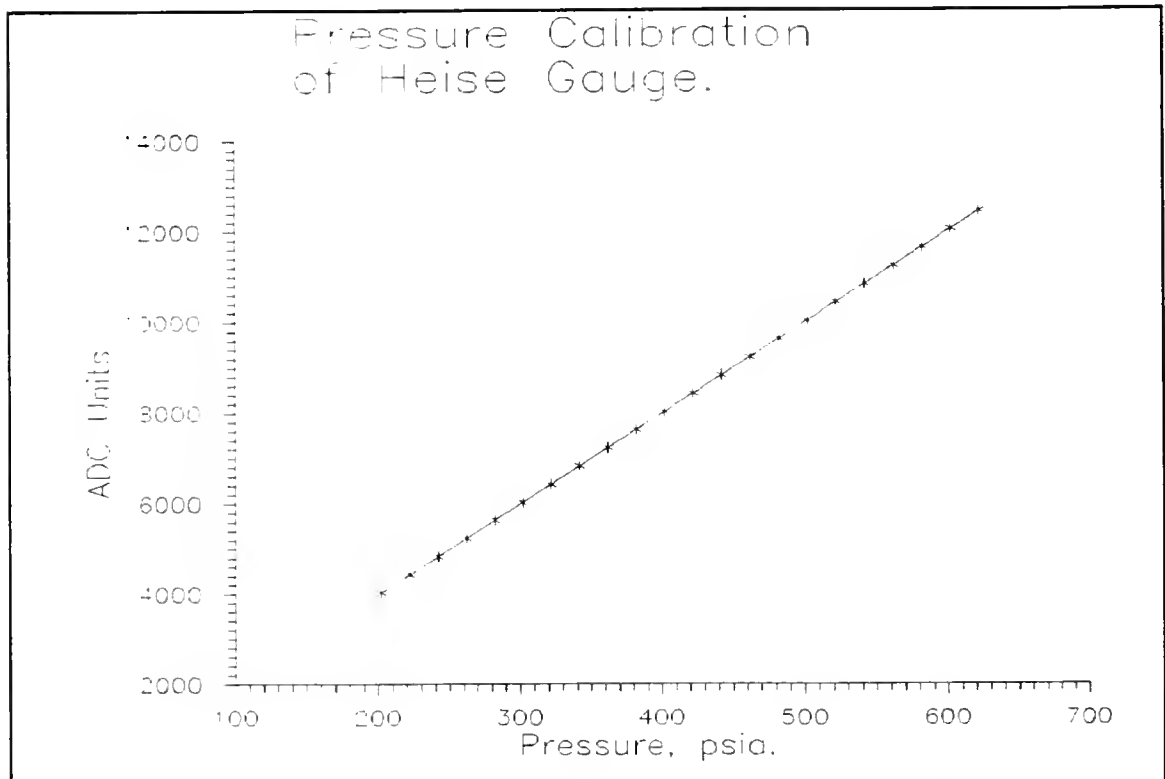


Figure 4-3. Calibration plot for the Heise gauge vs. ADC units.

System RTD Temperature Calibration

Two RTD's were utilized in the experiment. The isothermal environment RTD was used as a feedback device for the temperature control computer. The system RTD was used to measure the temperature of the fluid inside the resonator. Its response was recorded by the master data computer along with data related to pressure, volume and acoustic signal.

The system RTD received the closest scrutiny and underwent the most stringent calibration process.

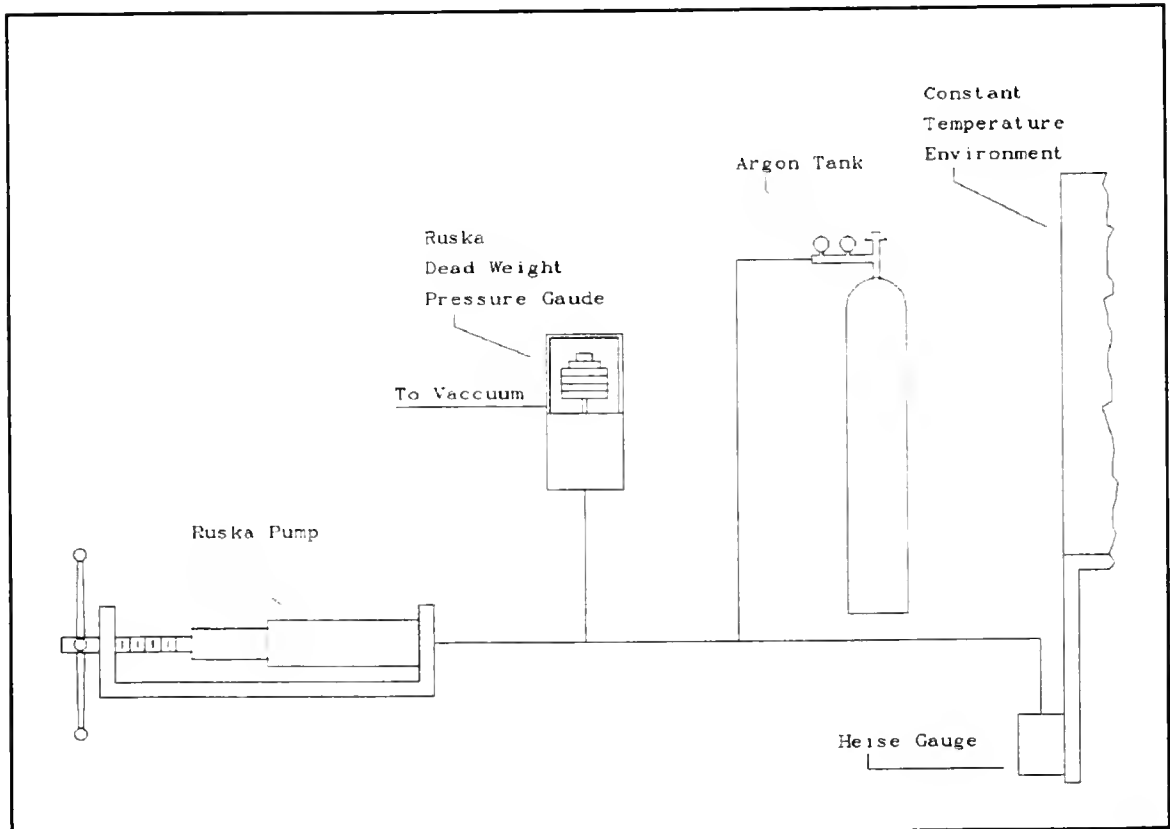


Figure 4-4. Pressure calibration setup.

A single platinum RTD was purchased precalibrated by its manufacturer and it complied with the guidelines set by the International Temperature Scale of 1990.²⁵ It came complete with α , β and δ coefficients for substitution into a standard equation relating the temperature to measured RTD values. It also came with a tabulation of resistance values for each degree celsius from -196°C to 260°C . This RTD was utilized as a laboratory standard against which others were calibrated.

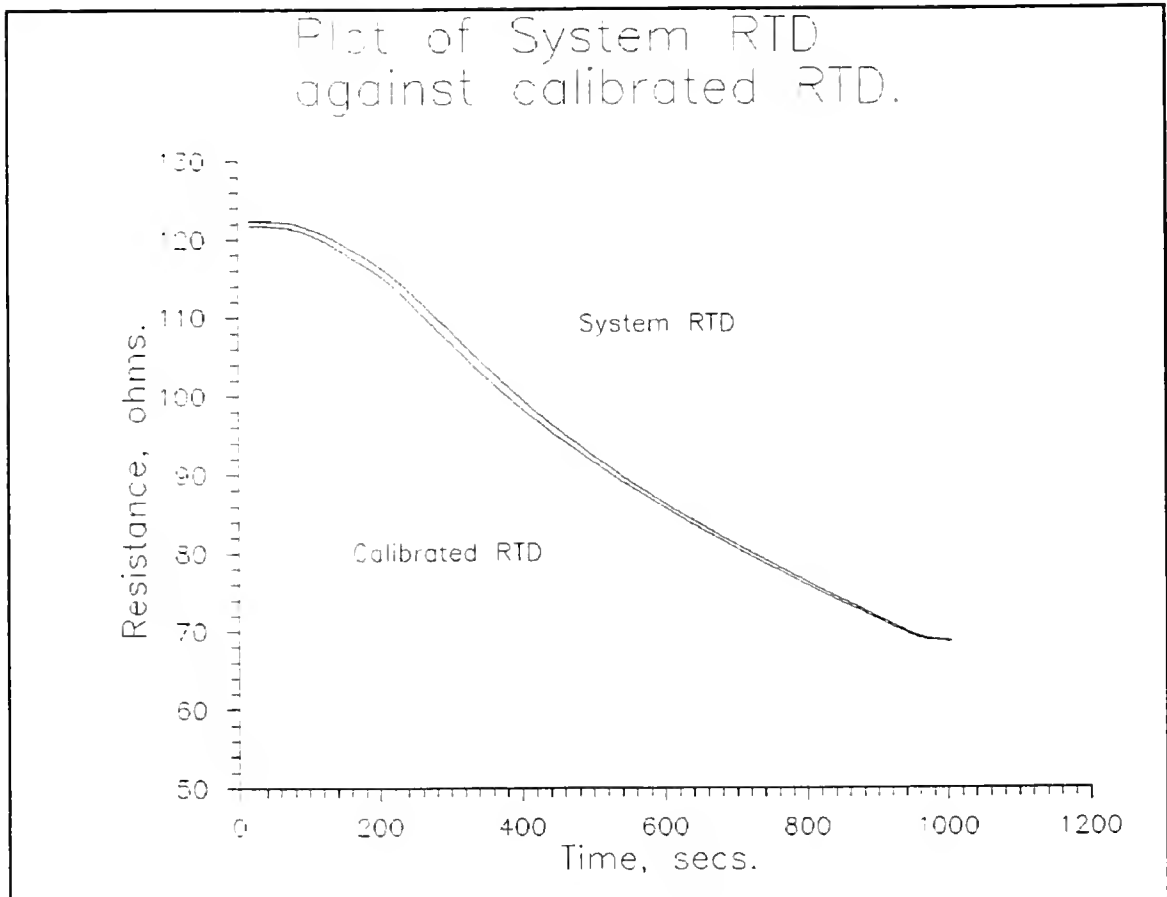


Figure 4-5. Response of system RTD and precalibrated RTD under identical conditions.

To ensure temperature calibration conditions were as close to experimental conditions as possible, both the environment and the system RTD were placed alongside the precalibrated RTD in the constant temperature environment. The temperature control computer was used to drop the temperature to the range of this experiment. Figure 4-5 shows the response of both the system RTD and the precalibrated RTD from room temperature down to experimental working temperatures. Figure 4-6 shows the resistance values of the system RTD plotted against the resistance values of the

precalibrated RTD. The slight departure from linear dependence is easily accounted for by a simple polynomial fit.

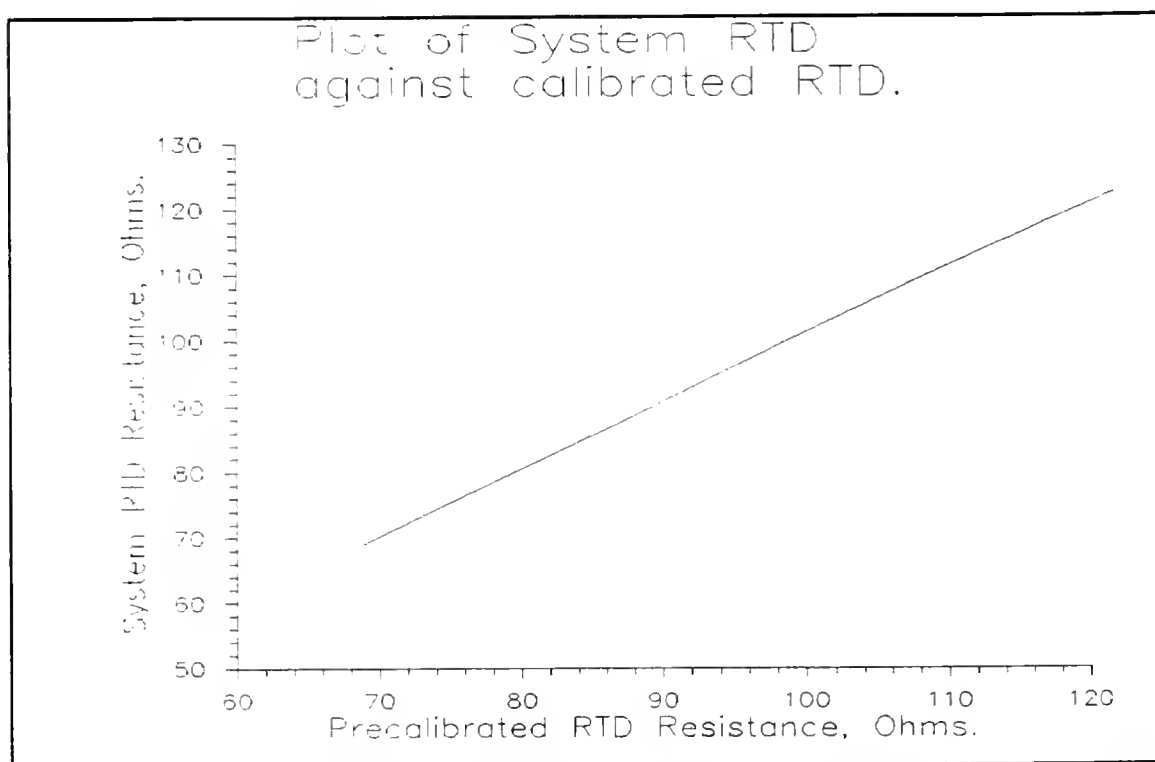


Figure 4-6. Plot of System RTD vs. Precalibrated RTD exhibiting strong linear response at low temperatures.

The precalibrated RTD was electrically connected to a Keithley 196A DMM. As a check of the DMM, the resistance of the precalibrated RTD was measured within a water triple point cell to ensure a resistance value that corresponded to a true temperature value. The triple point of water has been established as equal to 273.1600K.²⁶

Figure 4-7 is a plot of the resistance of the precalibrated RTD over time. The lowest resistance value corresponds to the temperature of the triple point of water.

Any difference between this lowest resistance value and the manufacturer's precalibrated value for the same temperature was treated as an offset due to DMM miscalibration. The offset amounted to a subtraction of 0.3529K from each recorded temperature value and was accounted for in all data tabulations.

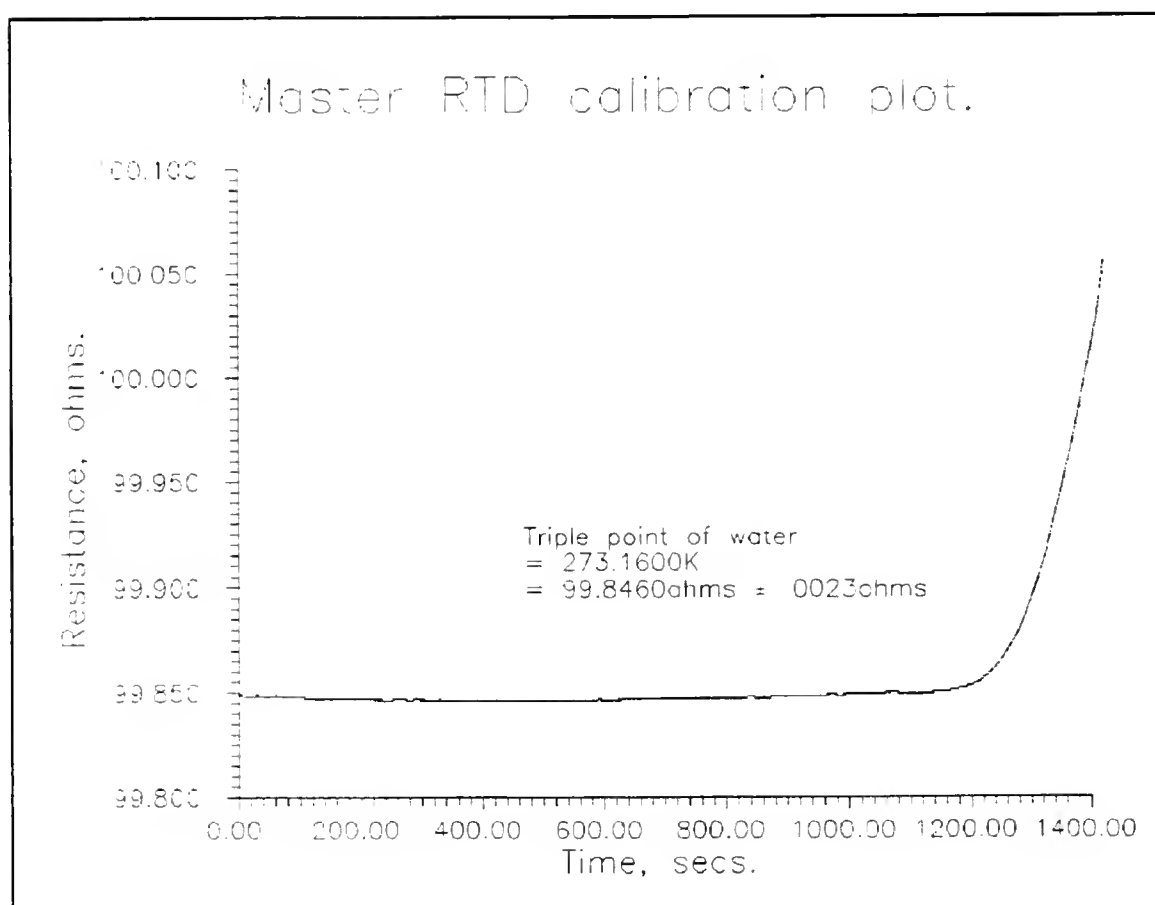


Figure 4-7. Triple point of water calibration for the precalibrated RTD.

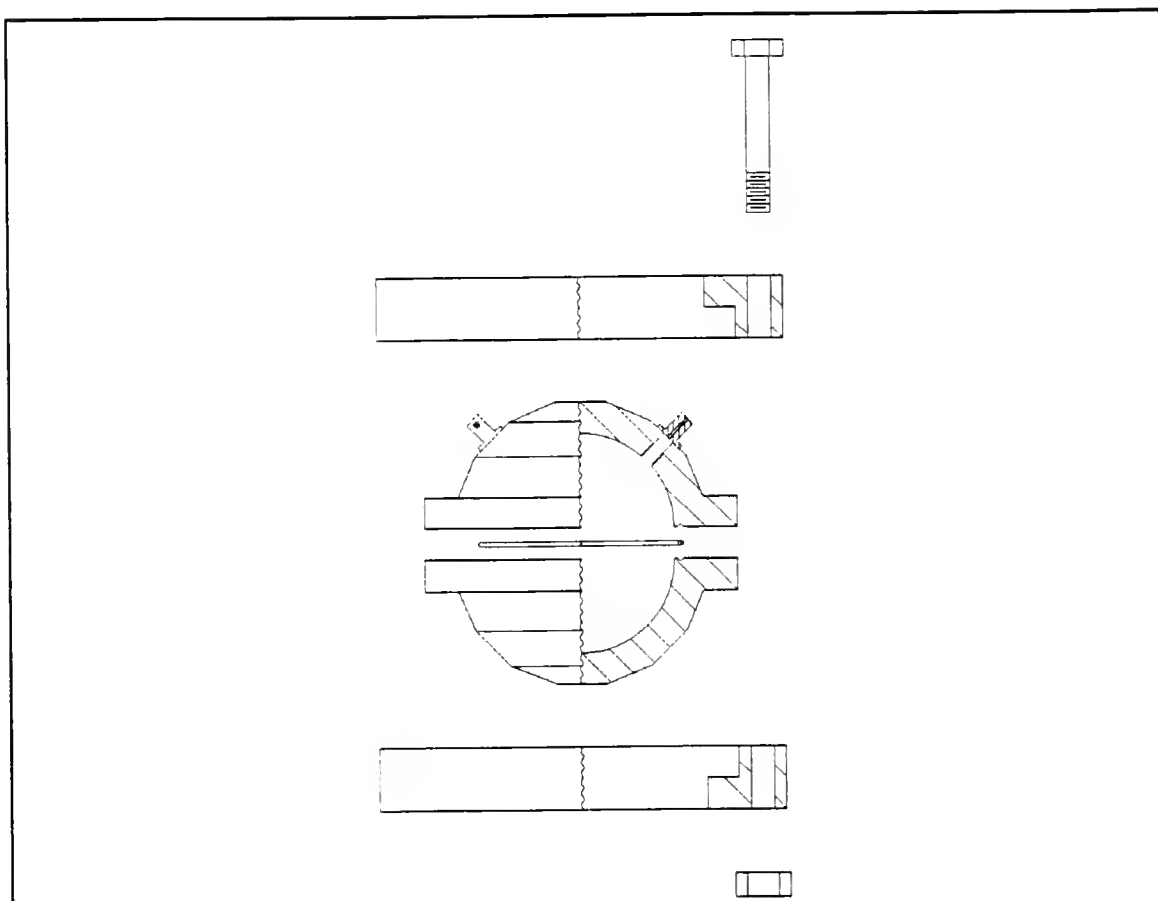
Apparatus DetailResonator

Figure 4-8. Spherical resonator schematic.

The heart of the apparatus, the spherical resonator was machined with the highest possible accuracy available. The six inch diameter resonator had a total diametral runout of .0001 inches. The construction was of type 304 stainless steel throughout. Figure 4-8 is a schematic of the resonator.

Resonator walls and the entire device were of quite substantial thickness, as operating pressures were near forty five atmospheres. Each time the liquid nitrogen tank was

being refilled, the apparatus was allowed to warm and the system pressure climbed as high as eighty atmospheres. To prevent the experimental apparatus from behaving as a bomb, the upper and lower collars shown in figure 4-8 were clamped together with twenty 3/8-24 bolts each torqued to one hundred foot pounds. The thin piece of material in the center of the drawing represents a copper gasket that sealed the two halves of the chamber together by being swaged into a groove in the upper and lower hemisphere.

Not shown in figure 4-8 are two small holes, one in the top of the chamber and one in the bottom of the chamber, which allowed fluids to enter and exit the chamber. The fluid used in the experiment was pumped continuously throughout the system to ensure good blending and prevent the development of temperature gradients. The actual system pump details have been documented elsewhere²⁷, but the pump circulated system fluid without generating strong pressure gradients.

Transducers

The transducers themselves were PZT bimorph oscillators .400 inches in diameter and .050 inches thick. Oscillation and frequency variation were induced by placing a variable electric potential across the excitation transducer. The transducers were located ninety degrees apart on a great circle. This arrangement subdues the response of many modes with a nodal plane perpendicular to the axis through the

sender, but does not interfere with the spherically symmetric radial modes, which are often the most favored signals. Since the radial modes of vibration are not affected by tangential interaction with the chamber walls, they are often the most attractive for scientific scrutiny. A transducer placement of ninety degrees gave the highest probability of clear reception of the most unperturbed modes of vibration within the sphere.

Proper mounting of the transducers within the chamber required careful attention. An electric signal had to be applied to or received from at least one side of the transducer. The stainless steel chamber itself could act as the electric potential return. The electric potential input had to be electrically shielded from the rest of the chamber and had to be mounted so as to withstand a pressure as high as 100 atmospheres. Also, the electrical and mechanical contact with the transducer had to have a low dampening effect else the vibrational signal strength would be poor.

A machinable ceramic, MACOR, was used to fabricate part of the transducer assembly. This material was elected for its structural strength, fluid impermeability and electrical insulating quality. A tapered ram plug was prepared from MACOR to match a tapered seat machined into the spherical chamber wall. A sheath of malleable copper with an integral elevated circumferential band was machined to fit between the ram plug and its tapered seat. Likewise, an electrically conducting pin was fabricated with another deformable band to

fit into a tapered hole formed coaxially in the ceramic MACOR plug.

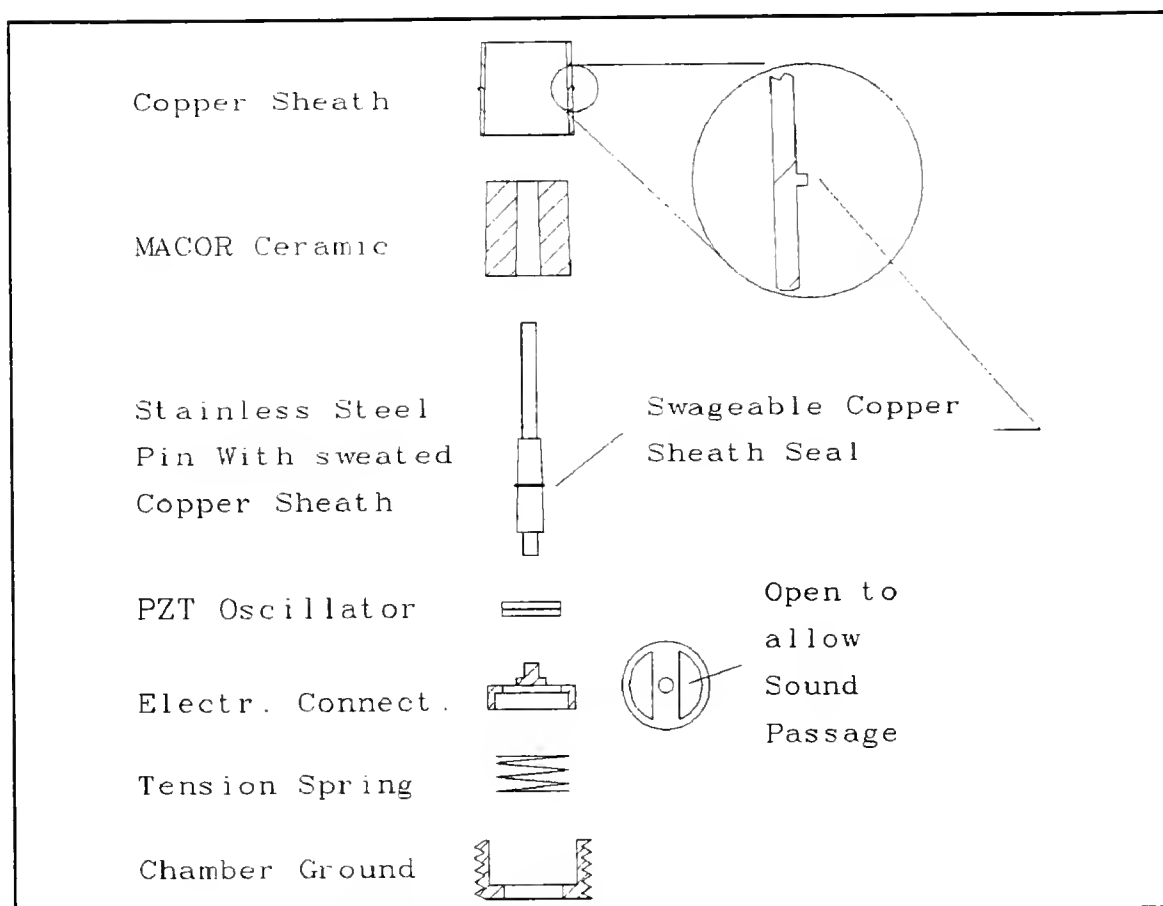


Figure 4-9. Construction detail for transducer mount.

The metal sheath, MACOR plug and centerline pin were assembled and pressed into the matching tapered seat with an applied pressure greater than the maximum pressure to be generated in an experiment. The action of pressing the assembly into the tapered opening swaged the fine metal rib back into the sides of the assembly and produced a strong hermetic seal. Figure 4-9 illustrates the transducer and feedthrough components.

Once an electrically isolated contact was provided, each transducer was supported top and bottom by an electrical contact at its center. Center transducer support was a novel mounting technique as previous workers had used the more common edge mounting technique. Center mounting allowed the transducer to float unconstrained except for the point contact. A vibrating circular membrane has a vibrational node directly at its center.²⁸ Therefore, transducer contact with the electrical connectors at the center of the transducer caused very little dampening effect. This arrangement proved to give better performance in terms of enhanced sensitivity and prolonged oscillator life.

System RTD Placement

The system RTD was placed within a shroud that was in direct contact with the system fluid. The system fluid was continuously moved through the shroud to ensure disruption of any potential temperature gradients. The shroud wall was made as thin as system pressures would allow to provide rapid thermal equilibration across the shroud barrier. Construction detail is illustrated in figure 4-10.

Bellows Construction Detail

A stainless steel bellows was used to provide a variable geometry for the system. The bellows was enclosed in a vessel built to withstand the full operating pressures present in the

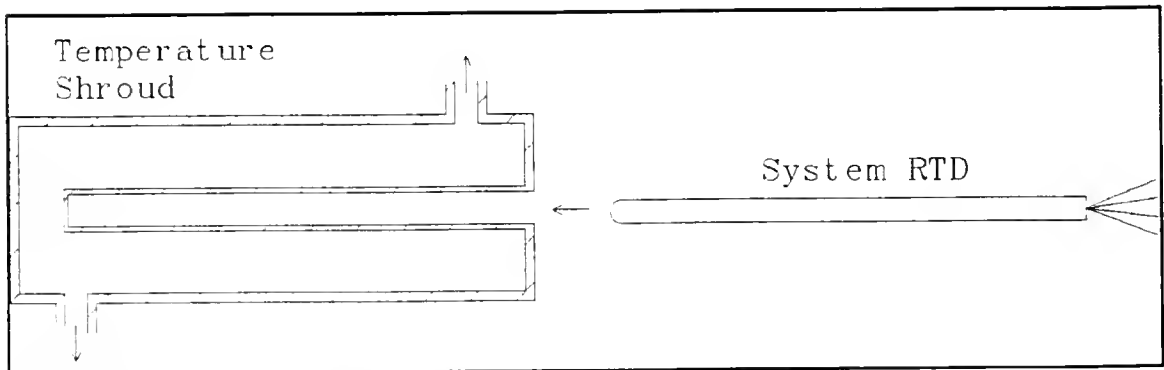


Figure 4-10. Construction detail of system temperature shroud.

experiment. The bellows itself, however, was fabricated from very thin material to allow flexibility. To keep the relatively fragile bellows intact at extreme pressures, fluids were introduced to both sides of the bellows at approximately equal pressures. System pressure was isolated on one side of the bellows while argon balancing pressure was isolated on the other side of the bellows. The thin material of the bellows walls was sufficient to contain the fluids on opposite sides provided the pressure difference never exceeded seventy psi. Approximately a thirty psi pressure difference from one side of the bellows to the other was enough to compress the bellows to its minimum position. System volume variation was achieved by slowly reducing the argon balancing pressure on the back side of the bellows. The system pressure was then able to push back the bellows and achieve an increased volume. Construction detail of the bellows is given in figure 4-11.

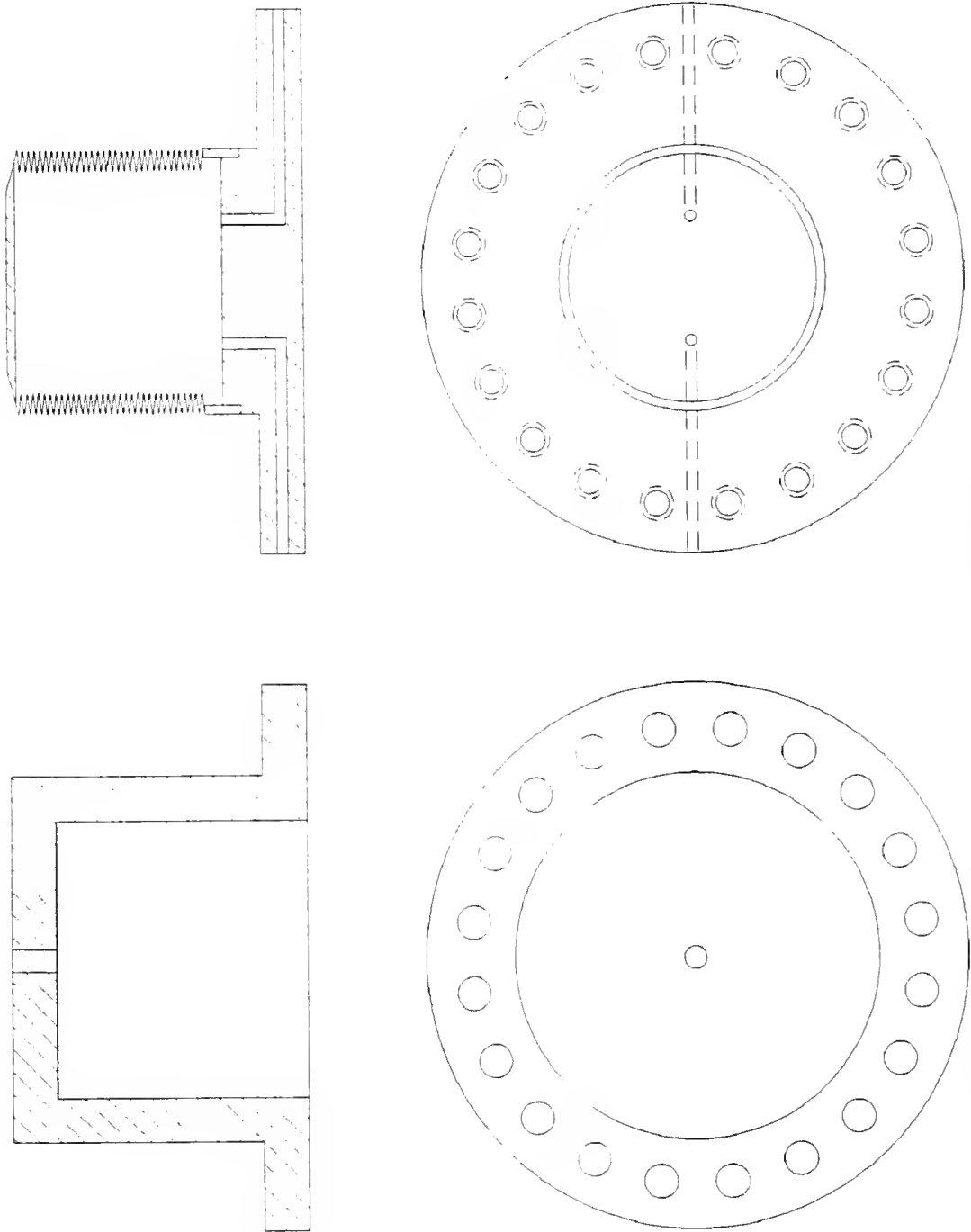


Figure 4-11. Construction detail of bellows assembly.

Instrument	Manufacturer	Model	Range of Operation	Accuracy	Use
Digital MultiMeter (DMM)	Keithley Instruments, Inc.	195A	4 terminal resistance measurement from $100\mu\Omega$ to $M\Omega$.	Range dependent. Owner's manual lists details.	Platinum resistance temperature device measurement
Digital MultiMeter (DMM)	Keithley Instruments, Inc.	196	4 terminal resistance measurement from $100\mu\Omega$ to $M\Omega$.	Also range dependent, but one digit better than model 195A.	System Platinum resistance temperature device measurement
Digital MultiMeter (DMM)	Keithley Instruments, Inc.	195A	4 terminal resistance measurement from $100\mu\Omega$ to $M\Omega$.	Range dependent. Owner's manual lists details.	LVDT position resistance measurement
Analog to Digital Converter (ADC)	IOtech	488/85	-10 to +10 volts i/o, 16 bit i/o.	$\pm 3\text{mvolts}$	Heise gauge and Acoustic spectrum voltage digitization

Table 4-1. Instrumentation Summary.

Instrument	Manufacturer	Model	Range of Operation	Accuracy	Use
Waveform Synthesizer & Function Generator	Hewlett Packard.	3325B	Sine wave from 1μHz to 21 MHz and amplitude of 10 volts peak to peak.	$\pm 5 \times 10^{-6}$ times a selected value at normal room temperature.	generates acoustic excitation sine wave and TTL square wave trigger synch.
Lock in Amplifier	Stanford Research Systems, Inc.	SR510	0.5Hz to 100 KHz.	± 10 volt output at full scale input.	Sine wave capture. Signal measurement down to 10nv full scale. Spurious strong signal rejection by using line notch and self-tracking bandpass filters.

Table 4-1. (continued)

Instrument	Manufacturer	Model	Range of Operation	Accuracy	Use
Pre-Amplifier	Stanford Research Systems, Inc.	SR560	0 to 250mv rms input.	1% gain.	Input noise reduction and full scale sensitivity extension to 10nv.
Oscilloscope	Leader, Inc.	1020	0 to 10 KHz frequency and 40 volt p-p amplitude display.	Vertical and horizontal drivers $\pm 3\%$.	Visual excitation or response sine wave follower.
Dynamic Signal Analyzer	Hewlett Packard.	H P - 35660A	488 μ Hz to 102.4Khz for single channel spectrum.	No details available.	4K real time fast Fourier spectrum display.

Table 4-1. (continued)

CHAPTER 5 RESULTS

Spherical Resonator

Spherical resonator development for the study of fluid speed of sound and related properties has been a successful activity of workers in this research group.²⁹⁻³⁸ There were, however, limitations in the previous work due primarily to construction of the spherical resonators. The earliest spherical resonator construction was of aluminum and designed to operate primarily near ambient temperature and pressure. Later, stainless steel was used as a construction material in order to study natural gas mixtures which contained small amounts of corrosive gases. These spherical resonators were designed to operate at moderate temperatures and pressures. They suffered from an imperfect spherical geometry due to fabrication methods used by the outside manufacturers.

The current apparatus incorporates several key features not found on earlier instruments. Newly added are thick wall design for high pressure work and exacting tolerances to ensure spherical geometry. Operating temperatures can be from approximately 77K to 525K. Operating pressures can extend from the lowest value that will still propagate an acoustic signal to 4000 psi. To ensure fluid purity and passivity,

stainless steel construction is used throughout the closed resonator system.

In addition to the extremes in operating conditions, the apparatus also incorporates a unique feature that allows the system volume to be varied. An expandable bellows assembly that varies the system volume up to 20% is an integral part of the apparatus. The addition of the bellows for the first time makes isothermal or isobaric studies practical. If isochoric work is desired, the bellows can easily be bypassed to yield a system with constant volume yet still capable of extreme operating pressures and temperatures. For this report, all work was done under controlled isothermal conditions.

Acoustic Spectra

A typical complete data set acquired in an isothermal volume scan included approximately 80-150 data points. Each datum point consisted of a value for temperature, pressure, and volume plus an entire acoustic spectrum. The acoustic spectrum consisted of a plot of signal amplitude versus signal frequency. Range and resolution for these two variables was 0-65535 units ± 1 unit and 0-10000Hz ± 0.15 Hz respectively. Figure 5-1 contains a typical acoustic spectrum taken from a data set collected well away from the critical point. Of particular interest is the apparent wealth of information contained within the spectrum. Signal amplitude is strong and frequency identification is straightforward.

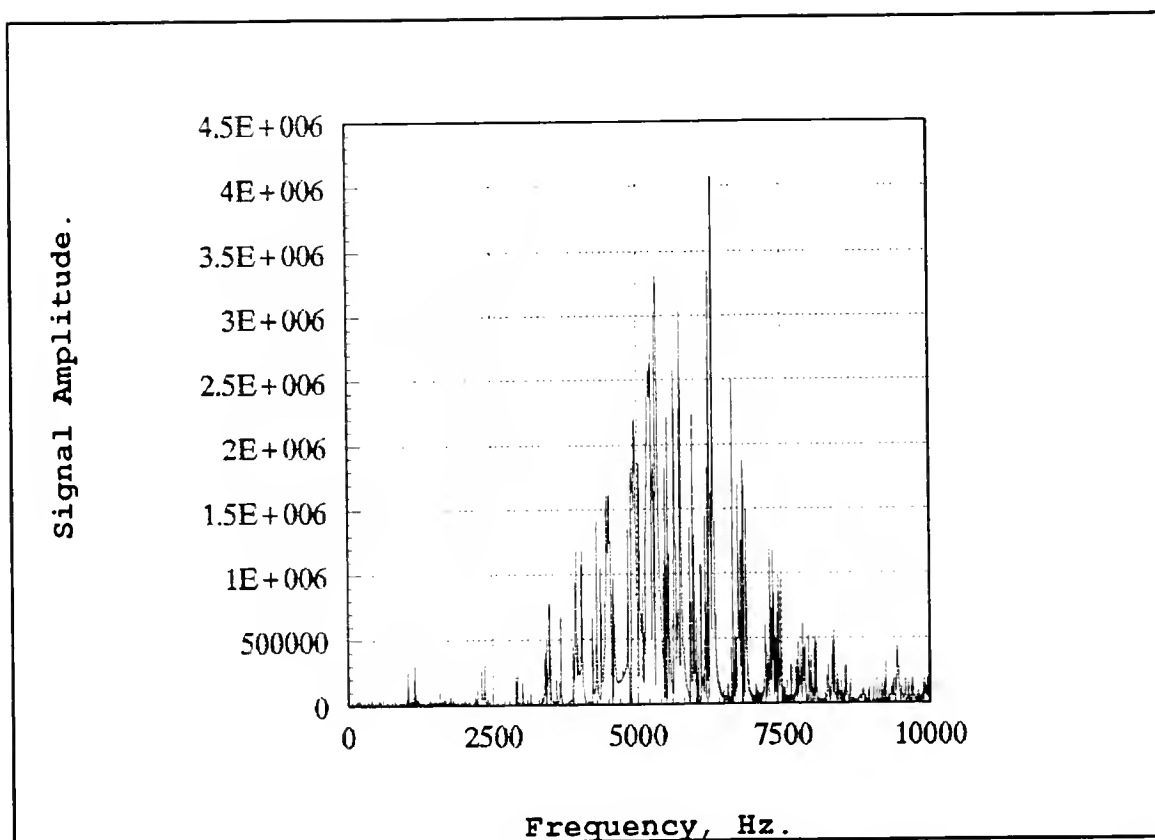


Figure 5-1. Typical acoustic spectrum recorded well away from the critical point.

Each spectrum was visually checked to identify the resonant vibrations by the method outlined in chapter three. Once identified, the third radial mode of vibration was tracked from spectrum to spectrum to follow the changing system speed of sound.

Figure 5-2 is an acoustic spectrum recorded very near the critical point. Notice the significant reduction in signal compared to figure 5-1. The most prominent signals in the spectrum appear at 60Hz intervals; these correspond to noise generated by the electric current supplied at the power outlet. However, the acoustic spectrum is still present, but

has been dampened by dispersion in the proximity of the critical point. Further analysis is consistent with a depressed sonic speed. Both the reduction in resonance amplitude and sonic speed are consistent with anticipated behavior near the critical state.

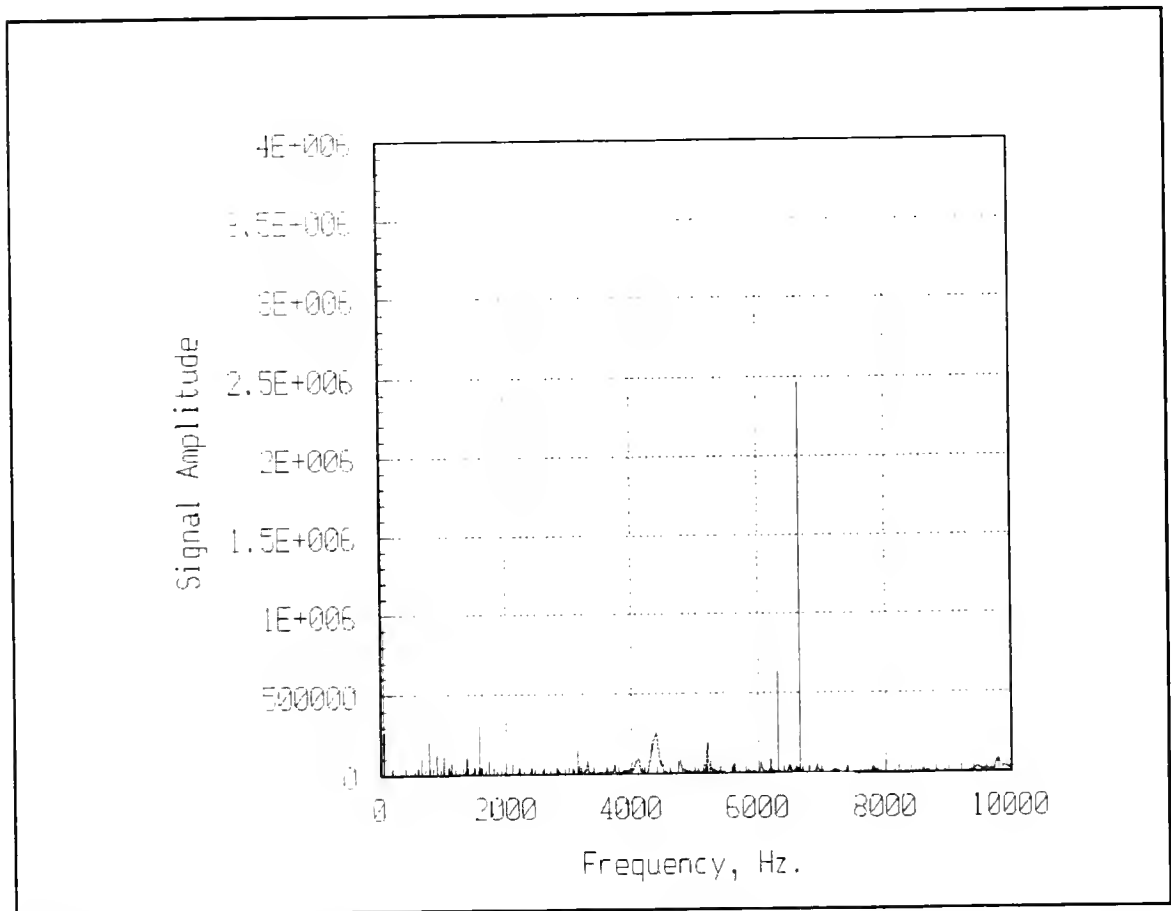


Figure 5-2. Typical acoustic spectrum recorded near the critical point.

Figure 5-3 and figure 5-4 are excerpts from two acoustic spectra taken from the same data set but separated by time and a change in system volume. Close examination of both spectra reveal that they have basically the same structure except that

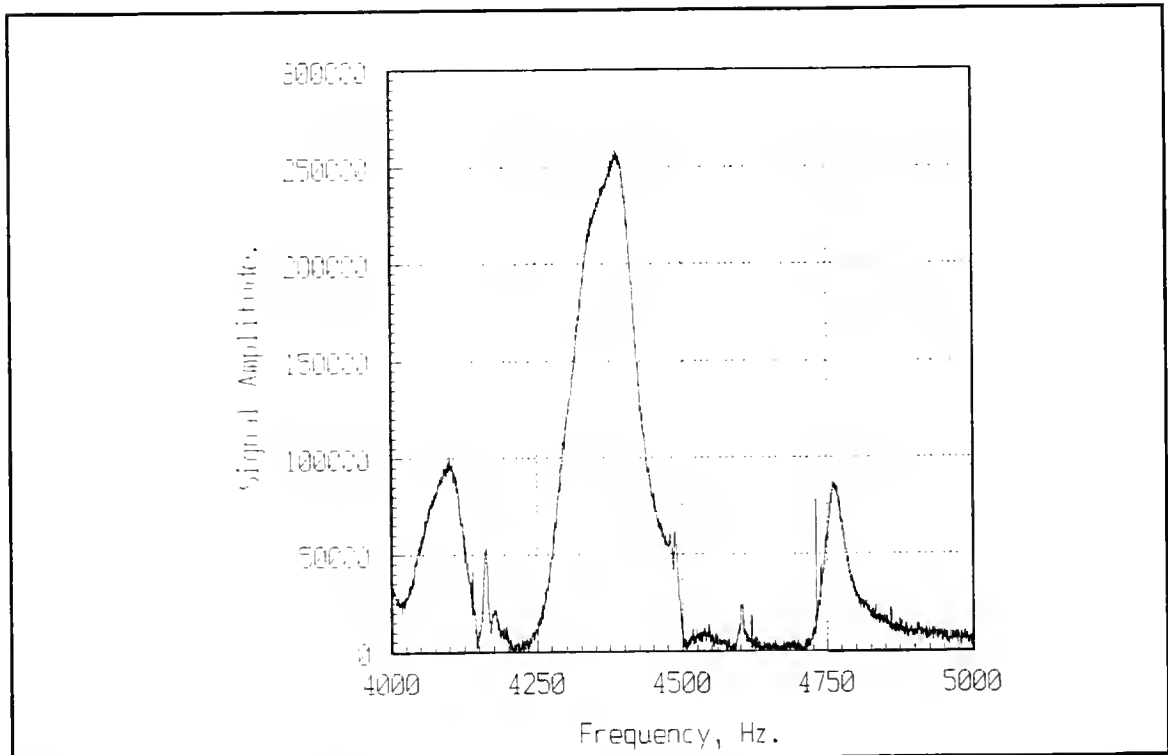


Figure 5-3. Excerpt from an acoustic spectrum near the critical point.

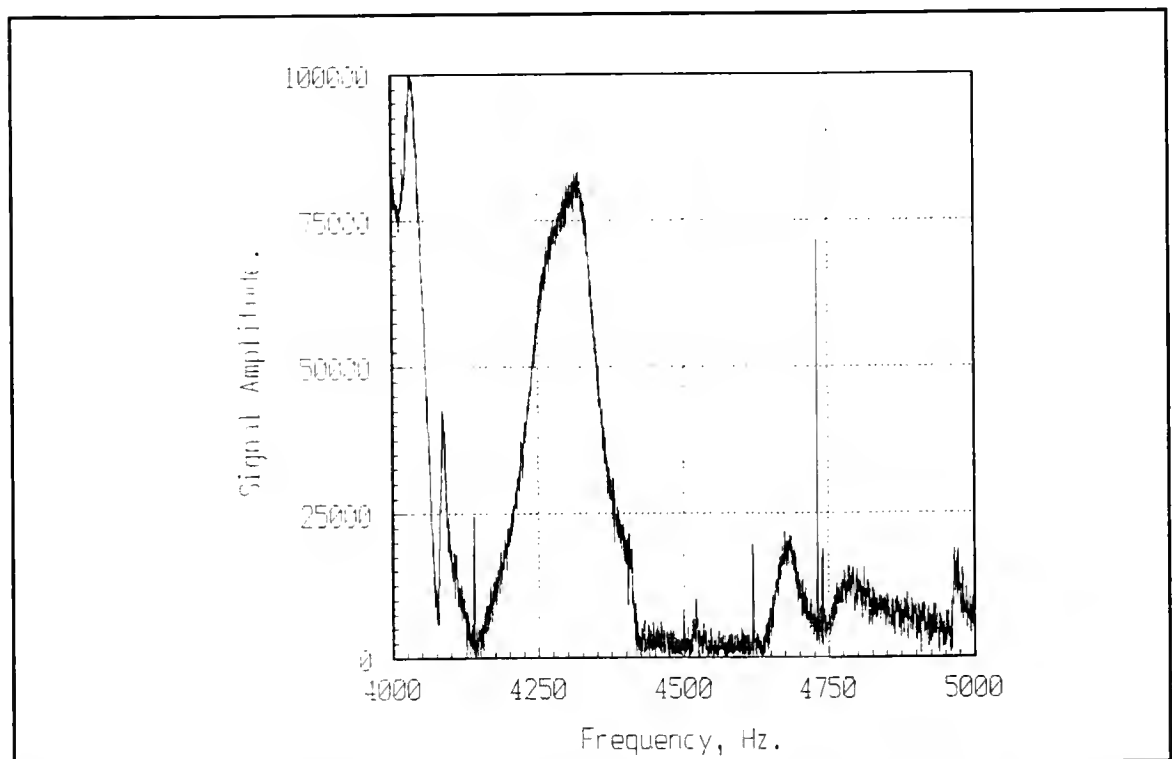


Figure 5-4. Excerpt from an acoustic spectrum after time and volume has changed, (frequencies are shifted toward zero frequency).

the second spectrum shows a shift toward zero frequency as well as an overall decrease in signal amplitude.

The frequency of vibration for a resonant peak is related to the system speed of sound according to eqn 3-21. In addition, the thermodynamic speed of sound becomes zero at the critical point. Therefore, the acoustic spectrum with the lowest frequency of vibration for a given resonant peak corresponds to the experimental conditions closest to the critical point for that data set. In figure 5-3 and figure 5-4, the peaks at 4612Hz and at 4517Hz respectively are each due to the third radial mode of vibration. The information in both spectra was recorded just two minutes apart at a change in system volume of only 0.1%. Clearly, the shift in the third radial mode vibration frequency is both dramatic and quantifiable.

Figure 5-5 is a superposition of both spectra excerpts and illustrates not only the frequency shift of the third radial mode but also the loss of signal amplitude that accompanies the approach of the critical point. The placement of the chamber transducers was designed to maximize the ability to identify the radial modes of vibration. Since the radial modes of vibration correspond to symmetric passage of sound toward and away from the chamber walls, they are the modes of vibration least subject to perturbation by transport effects and are, therefore, best suited for measuring the sonic speed.

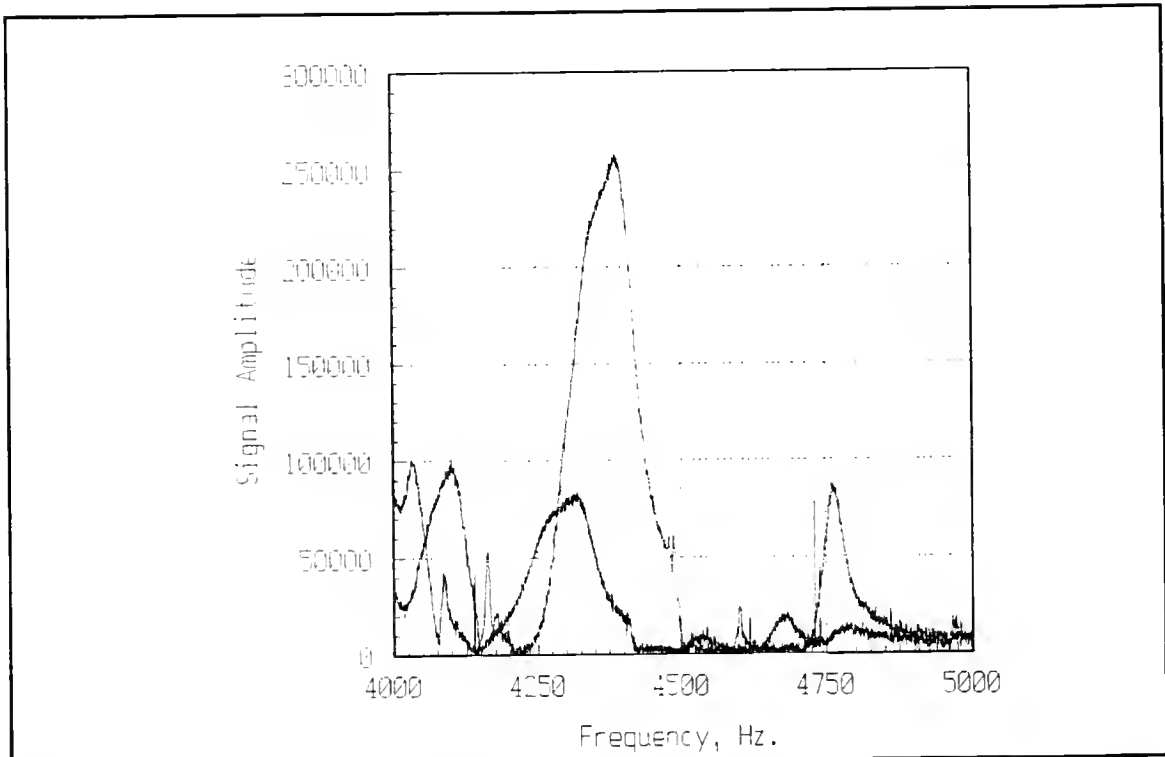


Figure 5-5. Superposition of two acoustic spectra excerpts illustrating the rapid change in resonant frequency and amplitude that accompanies a small change in volume near the critical point.

The third radial mode of vibration was utilized throughout the experiment for calculating the system speed of sound for two reasons. First, it is readily identifiable and well resolved from neighboring signals. Second, it has a large height to width ratio, (Q value), which makes it relatively easy to track from one acoustic spectrum to the next.

Data Manipulation

Each acoustic spectrum in the data sets was examined to find the peak corresponding to the third radial mode. The

frequency of vibration was converted to the system speed of sound, (see eqn. 3-21), and combined with the other system variables. A plot of system speed of sound versus system volume illustrates the relationship that exists between the two variables.

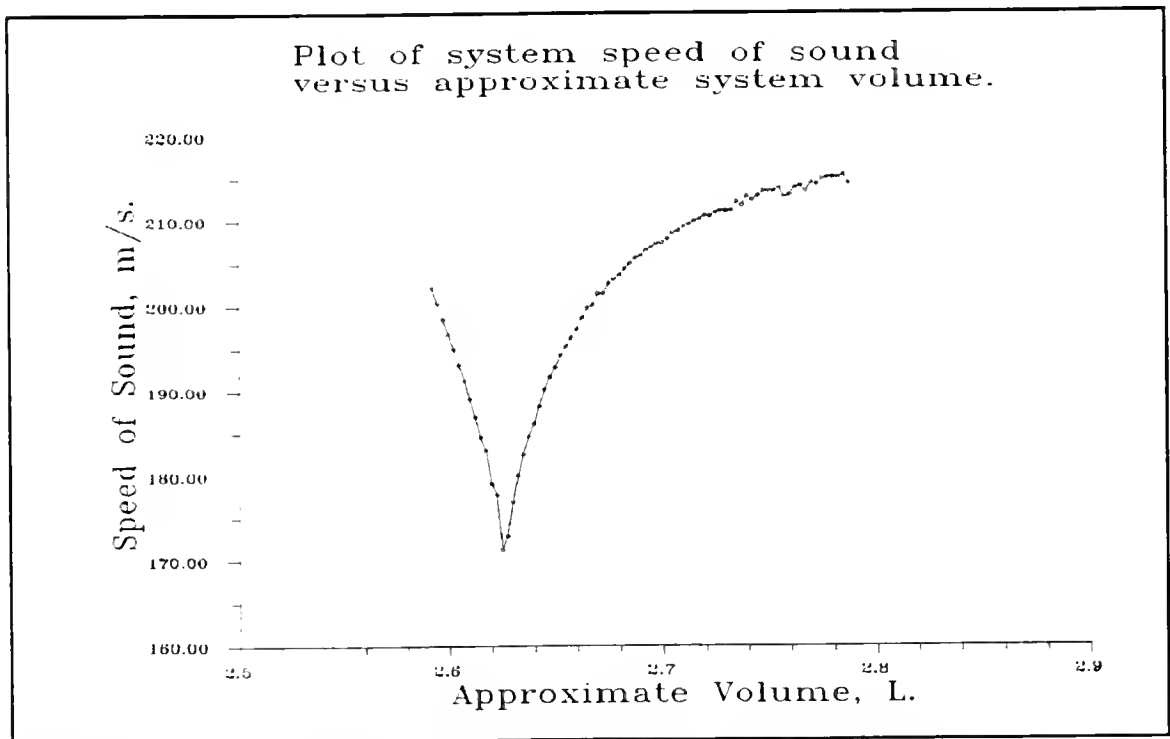


Figure 5-6. Typical relationship between system speed of sound and system volume near the critical temperature.

The allowed modes of vibration shift their frequencies strongly downward as the system density approaches the critical density. While at or near the critical temperature, the system speed of sound exhibits a similar behavior as it is directly proportional to the frequency of the allowed modes of vibration. Figure 5-6 illustrates the relationship between

the system speed of sound and the system volume under these conditions.

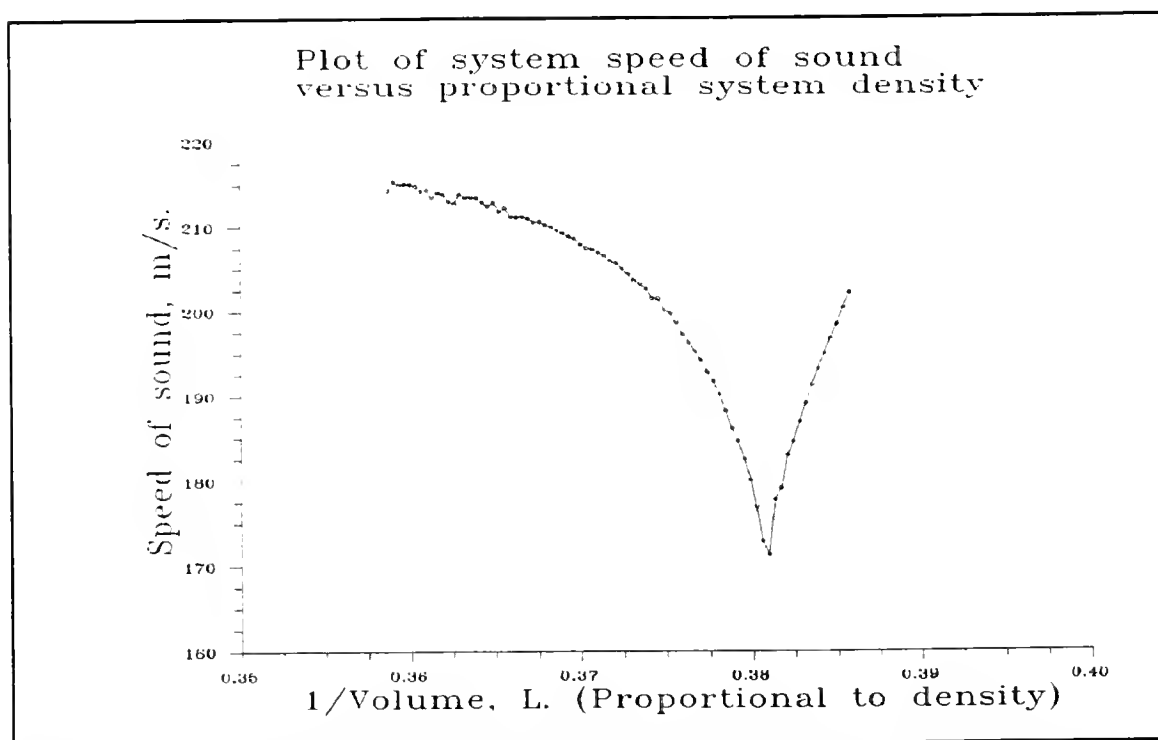


Figure 5-7. Typical relationship between the system speed of sound and the system density.

In a closed system, the molar density is inversely related to system volume by $\rho = \text{moles}/V$. Furthermore, the molar volume is defined as the volume occupied by a mole, $\tilde{V} = V/\text{moles}$. Therefore, the molar volume and molar density are inversely related, $\tilde{V} = 1/\rho$, and the data may be shown graphically in terms of density as in figure 5-7.

In both figure 5-6 and 5-7, the variable plotted along the x-axis is inexact. Originally, the experiment was designed to measure the system density analytically as well as the other system parameters. An elaborate method for weighing

the amount of methane introduced to the system was devised and fabricated. A calibration scheme for metering the exact system volume as a function of bellows position was also devised and put into practice. Unfortunately, a feature of the bellows that the experiment was built to exploit was also responsible for defeating the ability to measure the system density accurately.

The walls of the bellows were quite thin and flexible. As such, they allowed the bellows to move freely up and down and thereby change the overall system volume. When the bellows was at a low position, the walls were compressed and quite rigid. However, when the bellows was at a high position, the walls were uncompressed and had some freedom of movement to expand or bulge outwards. As the system temperature was changed, the stiffness or compliance of the bellows walls also changed. Therefore, the amount of the bellows outward bulge and the change in system volume changed dependent on temperature. The extra degree of freedom to bulge outward combined with changing wall properties based on temperature made it impossible to find an exact system density by monitoring the bellows position. Consequently, while the volume measurements illustrated in various graphs in this work are not highly accurate, they do not have an uncertainty of more than a few milliliters out of approximately a three liter system.

As the system volume was not precisely quantifiable, it is desirable to focus on a system parameter that was more accurately measured. The constant temperature environment was held to within ten millikelvin of each set temperature under study. The system volume was increased at a nearly constant rate and the system pressure and system speed of sound were tracked analytically.

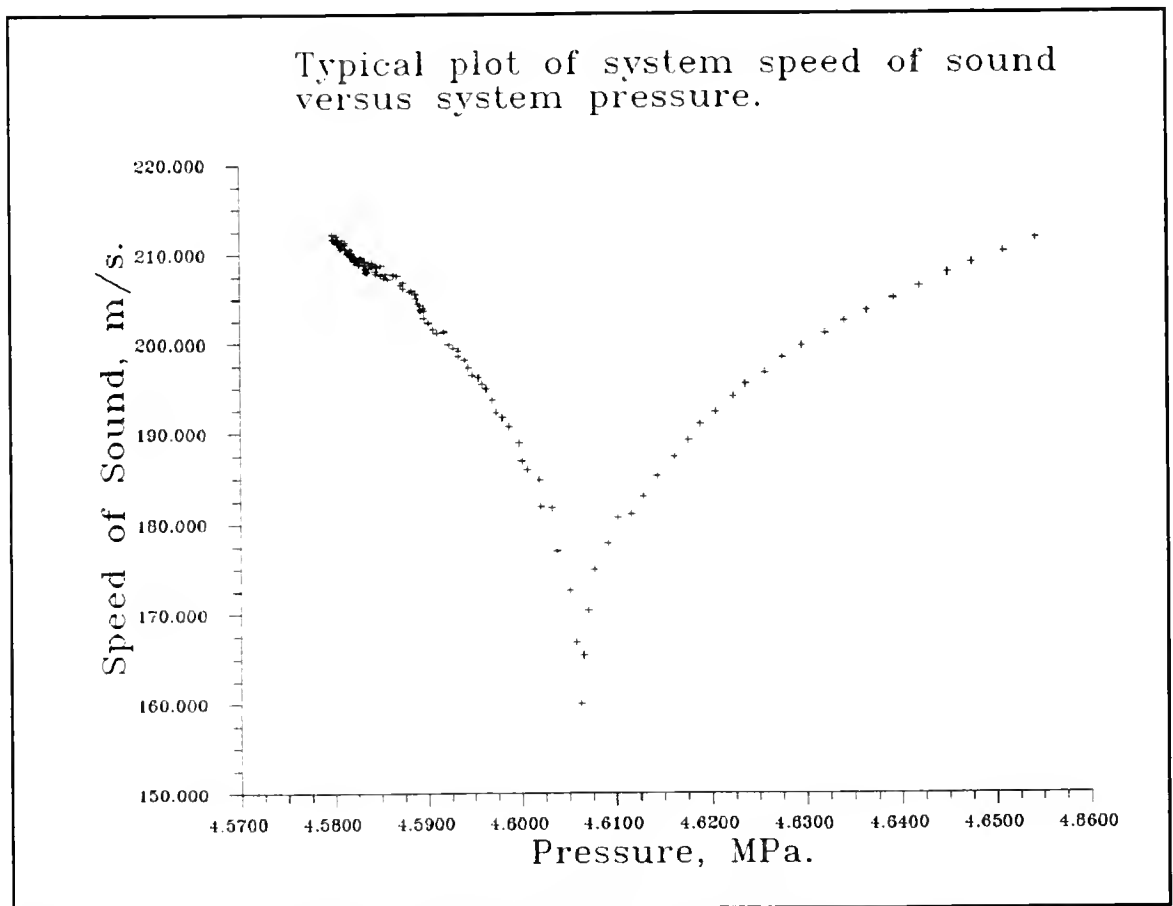


Figure 5-8. Typical relationship between the system speed of sound and the system pressure.

Figure 5-8 is a plot of system speed of sound versus system pressure. The minimum that appears at the center of the graph corresponds to the closest approach to the critical point recorded by the system parameters; that is the pressure, volume, temperature and the speed of sound within the enclosed methane.

Figure 5-8 may be roughly divided into two parts. To the left of the minimum, the system pressure is less than the critical pressure and the system exists as a single gaseous phase fluid. In this region, the system speed of sound is inversely proportional to the system pressure. As the pressure is increased, the speed of sound is decreased. To the right of the minimum, the system pressure is greater than the critical pressure and the system exists as a two phase fluid of gas and liquid in equilibrium. In this region, the system sonic speed is directly proportional to the system pressure. As the pressure is increased, the speed of sound is also increased.

Each plot of system speed of sound versus system pressure can be examined for the location of the minimum. Since the thermodynamic speed of sound goes to zero at the critical point, the individual plot with the minimum that extends to the lowest system speed of sound corresponds to the experimental conditions closest to the conditions that exist at the critical point. It is possible to make each plot on a single set of axes and thereby readily identify the single

plot that most closely approaches the critical point conditions. At the same time, an indication of the precision of the overall technique can be demonstrated.

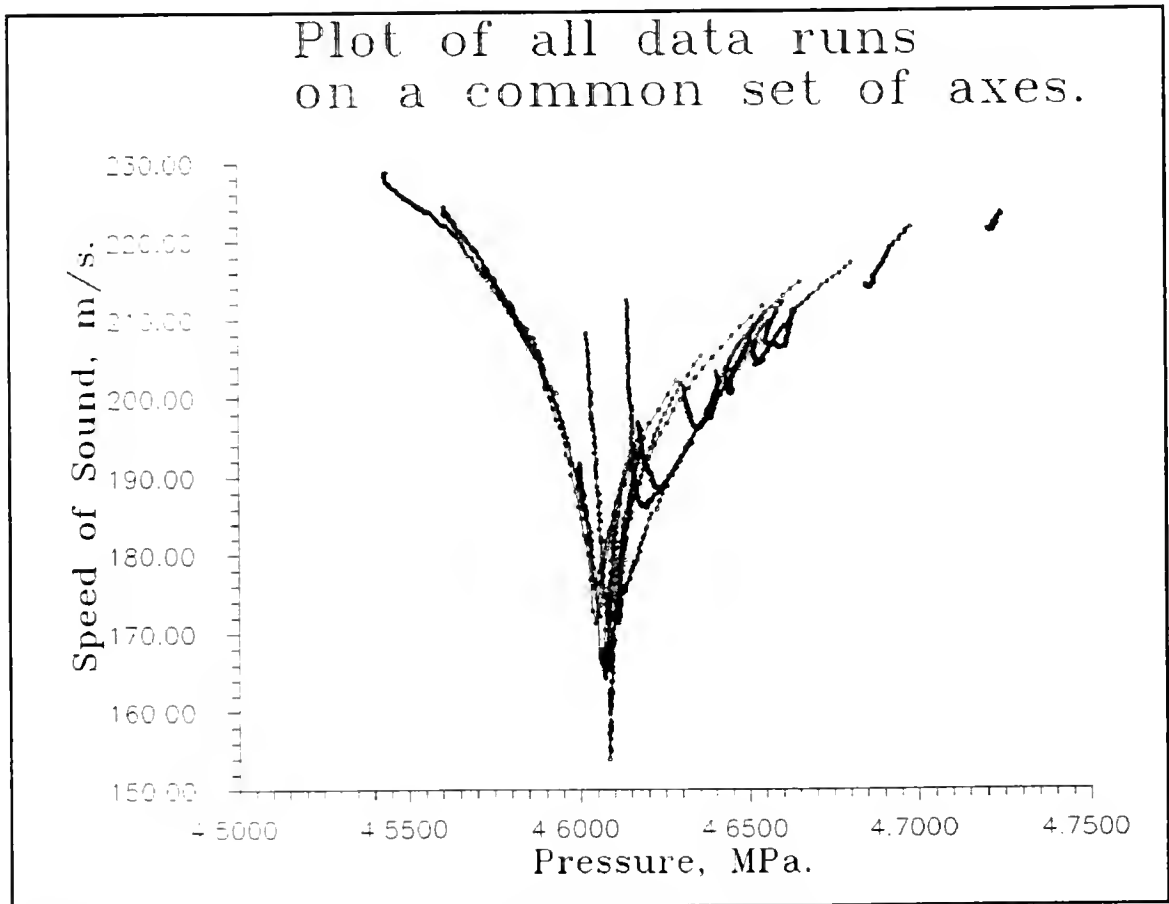


Figure 5-9. Plot of all data sets of pressure and speed of sound on a common set of axes.

Figure 5-9 illustrates the asymptotic nature of system speed of sound as the experimental conditions approach the critical point conditions. Combined in the plot shown in figure 5-9 are a total of twenty data runs consisting of 2487 total data points. As the critical point is approached, the combined plot rapidly falls off toward zero speed of sound and

exhibits a 'spike' pointing to the pressure that corresponds to the critical pressure.

While it is true that the system speed of sound never reaches zero, the inaccuracy of identifying the critical point is very small. The asymptotic behavior exhibited by the speed of sound at the critical point provides a strong indicator of the critical pressure that precludes the necessity to attain zero speed of sound.

All data for this experiment were to be collected under isothermal conditions. The constant temperature environment was kept at a set point temperature to within ten millikelvin for each data run. However, the temperature within the fluid system itself did not remain nearly so constant. Even though it was possible to maintain a very constant temperature around the sealed spherical resonator, the fluid inside the system was isolated enough that temperature variation was as much as several hundred millikelvin over the course of a single data run. Figure 5-10 illustrates the temperature variation within the sealed spherical resonator as a function of time during a data collection run.

It is apparent from figure 5-10 that it was difficult to maintain isothermal conditions during a data collection run. Again, one of the strengths of the system was also one of its weaknesses. The movement of the bellows created an expanding system volume and also generated a system temperature drop. This effect commonly occurs when a gas is allowed to expand

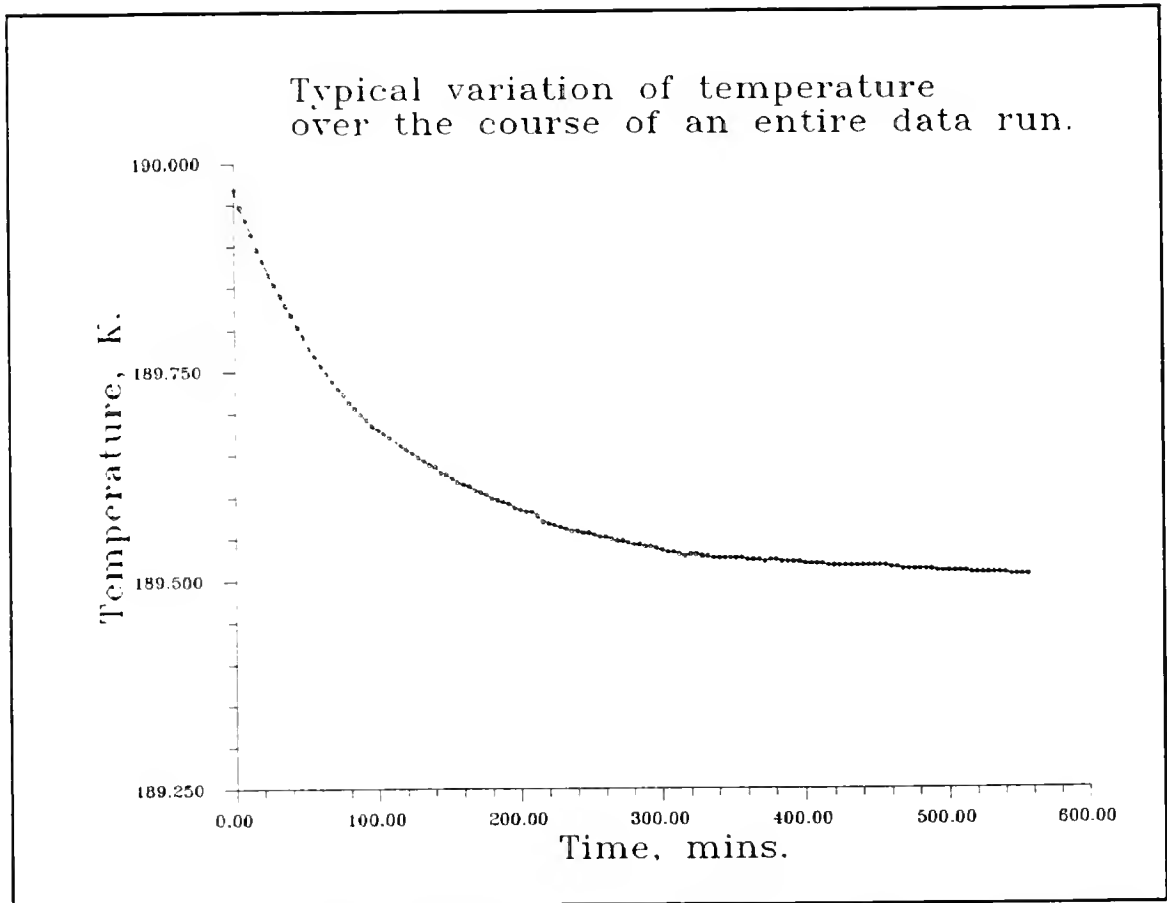


Figure 5-10. Largest temperature variation for a single data run.

and do work against the surroundings. The process is essentially adiabatic since the exchange of heat across the phase boundary represented by the solid system walls is very slow.³⁹ The loss of internal energy that accompanies the expansion of the thermodynamic fluid is reflected in an overall drop in system temperature. The only way to prevent such a phenomena would be to provide a sufficient amount of heat exchange to ensure constant system temperature. The thick wall design of the resonator system that allowed high pressure work also provided sufficient insulation to mitigate against a constant temperature under volume ranging

conditions. Consequently, all experiments were carried out under approximate isothermal conditions only. A more efficient heat exchange system would have to be provided for future work to approximate isothermal working conditions more closely.

Such a situation does not negate the results of the experiment, because the system temperature was recorded throughout data collection. A plot of system pressure or system speed of sound versus temperature should appear as a vertical line if true isothermal conditions are maintained. Figures 5-11 and 5-12 illustrate the departure from isothermal conditions typically encountered in this work.

Figures 5-11 and 5-12 represent the worst case of departure from isothermal run conditions. In general, the drift in temperature during a run averaged approximately 0-1K, but even this made the ability to zero in on the critical temperature very difficult. Typically, a temperature had to be selected for the constant temperature environment that was about a tenth of a degree higher than the temperature of interest in order to be assured of being near the proper temperature when the system expanded sufficiently to be at the critical density. A task that was difficult at best and one that required some trial and error to produce reasonable results.

A plot of system speed of sound against system temperature for all data runs should produce a series of

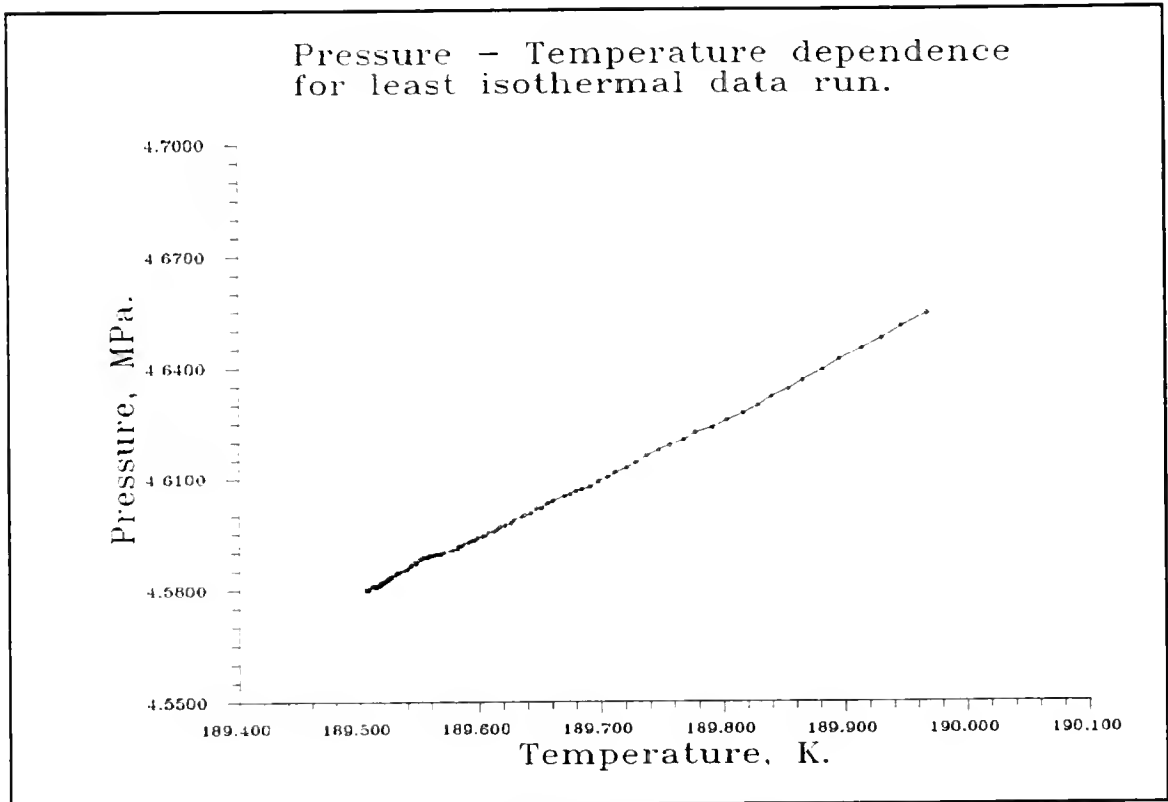


Figure 5-11. Pressure dependence on temperature for data run that deviates most from isothermal conditions.

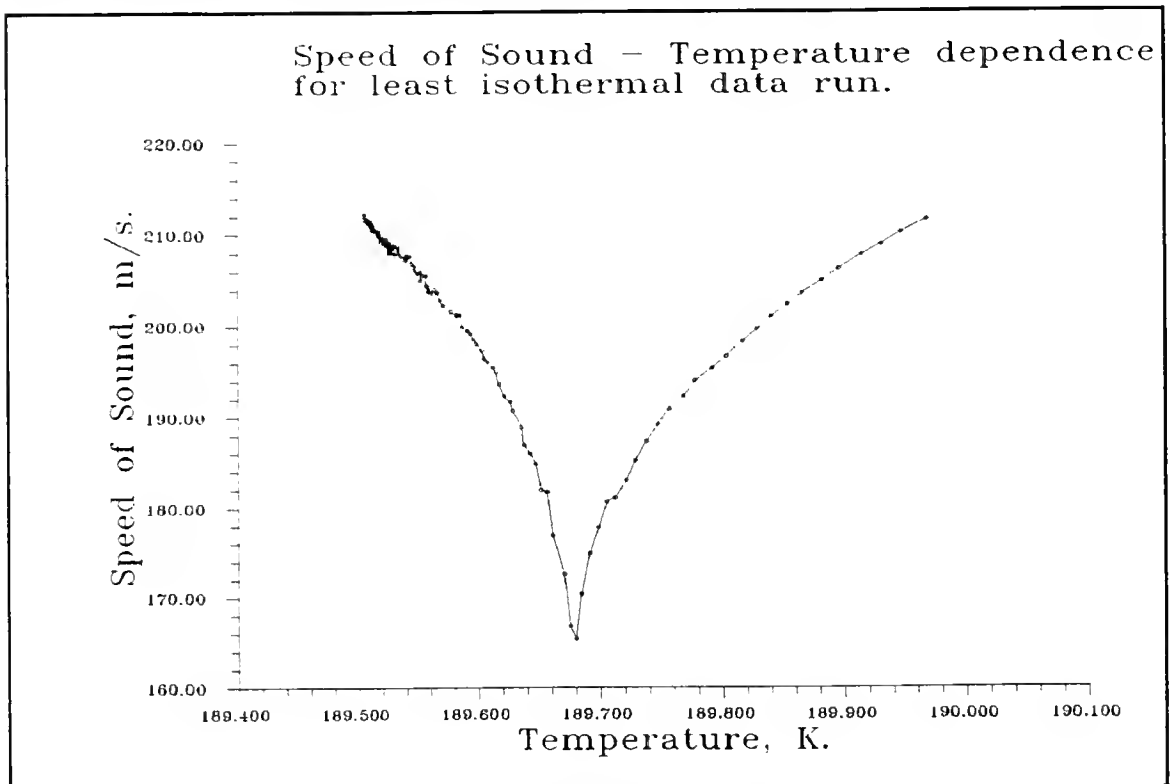


Figure 5-12. Frequency dependence on temperature for data set that deviates most from isothermal conditions.

vertical lines, provided the system was truly operating under isothermal conditions. A slight drift in temperature should produce a series of v shaped curves as the system speed of sound decreases, reaches a minimum and then increases when the critical density is approached, passed and moved away from. Figure 5-13 is a plot of system speed of sound versus system temperature for all data runs. Inspection shows that every data run experienced a temperature drift during the course of an experiment. No amount of time was sufficient to ensure true thermal equilibrium with the constant temperature environment.

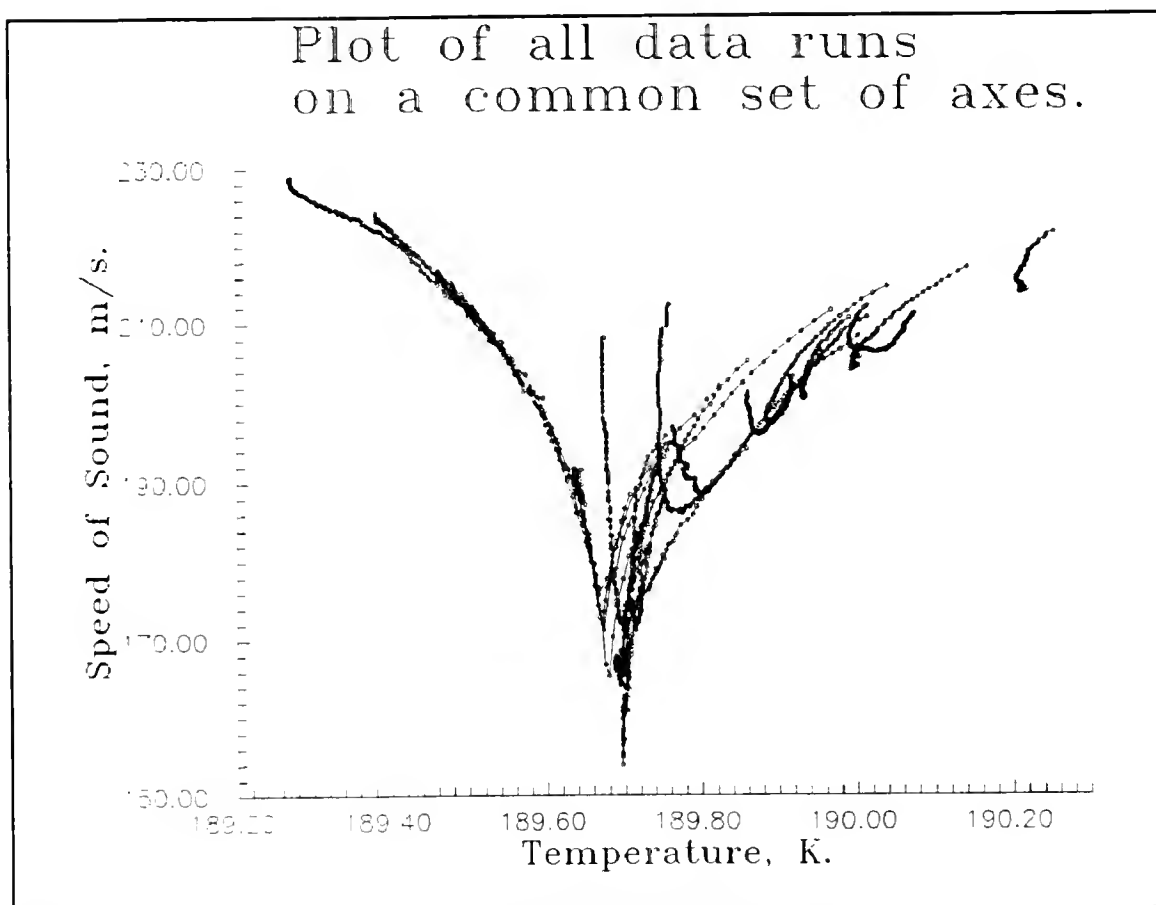


Figure 5-13. Plot of all data runs of system speed of sound vs. system temperature on a single set of axes.

A three-dimensional plot of all three system parameters clearly demonstrates the precision of the technique employed in this experiment. Figure 5-14 is a plot of system speed of sound, system temperature and system pressure. The plotted figure looks strikingly like the head of an arrow pointing directly to the critical point. No other technique provides such a striking indicator of the location of the critical point.

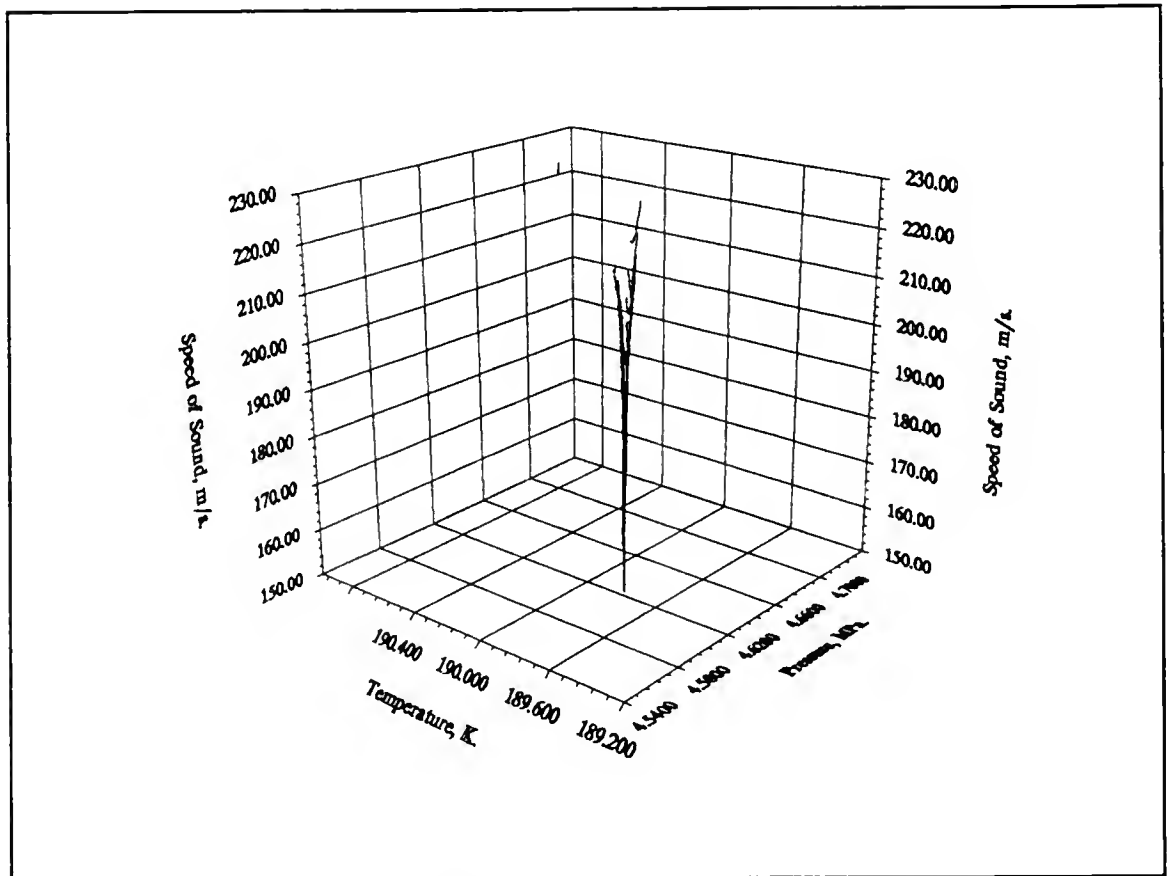


Figure 5-14. Three dimensional plot of system variables; pressure, temperature and speed of sound.

Curve Fitting

To attain the parameters for the critical point of methane, it is possible to draw the limiting slope asymptotes on figures 5-9 and 5-13 and identify their intersection as the critical point. However, such a technique is graphical in nature and subject to individual interpretation. Since the overall experimental technique is based on a mathematical singularity, a much more satisfying method of critical point identification would involve a fit of the experimental data to an appropriate mathematical relationship from which the critical parameters may be analytically inferred.

Critical pressure

A model for describing the behavior of the latent heat of vaporization as a function of temperature was proposed by Stell and Torquato.⁴⁰ Their mathematical model and subsequent equation was modified by Sivaraman et al.^{41,42} to relate the speed of sound to temperature. The equation was derived from renormalization group theory by Wegner⁴³ and later refined by Ley-Koo and Green.⁴⁴ The mathematical model treats behavior similar to that exhibited by the experimental data gathered from this work. The basic equation relating speed of sound to temperature is

$$\frac{C}{\sqrt{\frac{RT_c}{M}}} = \frac{A_1 T_r^\beta + A_2 T_r^{\beta+\delta} + A_3 T_r^{1-\alpha+\beta} + A_4 T_r + A_5 T_r^2 + A_6 T_r^3}{\quad} \quad \text{Eqn. 5-1}$$

Where c = Speed of Sound, m/s
 R = Ideal Gas Constant, J/(K)mole
 T_c = Critical Temperature, K
 M = Molecular Weight, Kg/mole
 A_i = Coefficients
 T_r = Reduced Temperature ($|T - T_c| / T_c$)

Equation 5-1 is utilized to fit data on either side of the critical temperature. The equation contains ten system dependent variables that must be found such that the overall deviation of the function from experimental values is minimized. The quantity represented by the square root symbol in equation 5-1 has units of m/s and renders the left side of the equation unitless. Since the reduced temperature has no units associated with it, each of the variables on the right side of the equation is also unitless.

For work conducted under isothermal conditions, Eqn. 5-1 can be modified to work with pressure instead of temperature. Wherever the reduced temperature appears, the reduced pressure can be substituted. What constants should appear under the square root symbol on the left side of the equation is unclear, but they must combine to yield a quantity that has the units of m/s to assure that the left side of the new equation is also unitless. A simpler process is to cross multiply both sides of the equation by the quantity represented by the constants under the square root symbol and

allow the coefficients on the right side of the equation to have the units of m/s. Equation 5-1 can then be rewritten as

$$C = A_1 P_r^\beta + A_2 P_r^{\beta+\delta} + A_3 P_r^{1-\alpha+\beta} + A_4 P_r + A_5 P_r^2 + A_6 P_r^3 \quad \text{Eqn. 5-2}$$

Equation 5-2 has only nine system dependent variables to be searched instead of the ten of equation 5-1. Equation 5-2 will not yield a value for the critical pressure directly, but the nine system dependent parameters can be found utilizing an estimated value for the critical pressure. The critical pressure can then be varied and the nine system dependent parameters recalculated. Overall equation deviation can be compared from one iteration to the next until the error has been reduced to a minimum. The final value for the critical pressure is taken as that value which produces the minimal deviation of the fitted equation from measured experimental results.

The visible cross hatches in figure 5-15 are the actual experimental data for a single data run while the smooth line represents the results of fitting equation 5-2 to all the data. It can be readily seen that the fitted equation reproduces actual experimental results very closely. The nine system dependent variables are reproduced in table 5-1 along with the value for the critical pressure which yields the smallest deviation of the fitted equation from actual

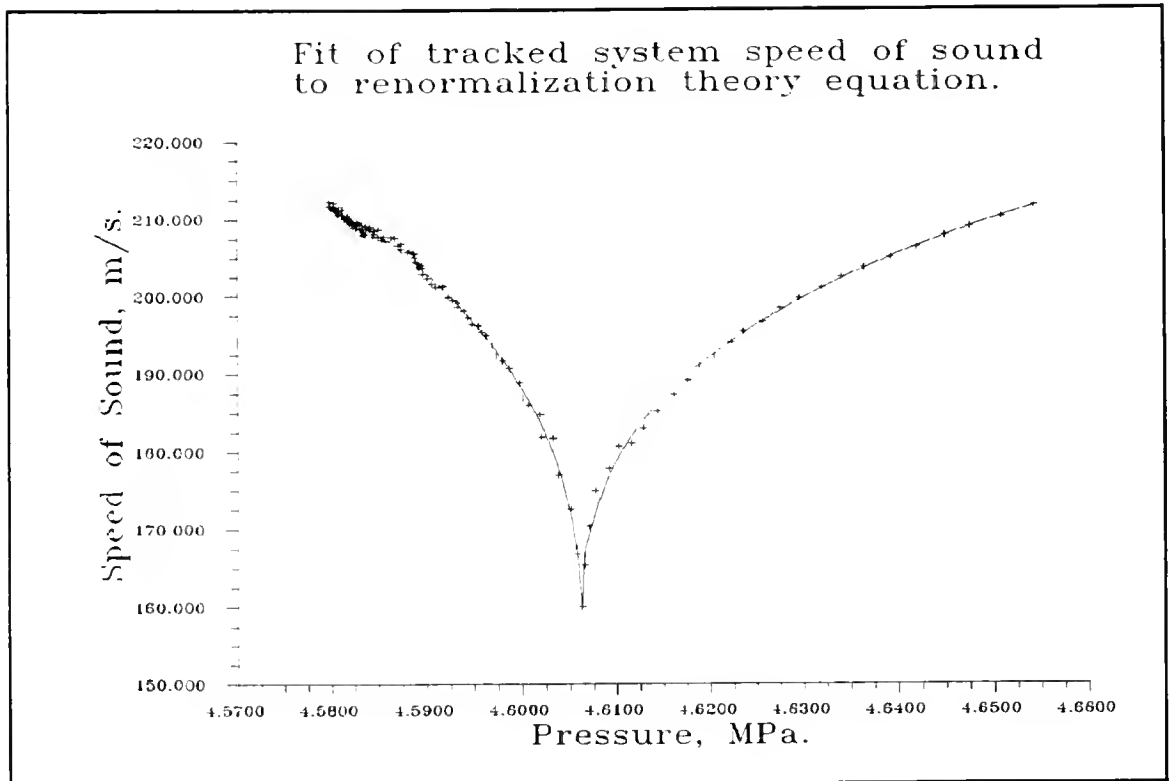


Figure 5-15. Plot of system speed of sound versus system pressure with fitted equation overlaid.

experimental results, (chi squared from the regression analysis was 0.9972).

A close examination of the exponents on P_r in eqn. 5-2 indicates that $\beta + \delta = 1$. However, another exponent on P_r is already 1. Thus, both terms can be combined to simplify equation 5-2. Yet, the coefficients in front of these same two variables are equal in magnitude but opposite in sign which suggests they cancel each other out. Consequently, equation 5-2 reduces to the simplified expression shown in equation 5-3.

$$C = A_1 P_r^\beta + A_3 P_r^{1-\alpha+\beta} + A_5 P_r^2 + A_6 P_r^3 \quad \text{Eqn. 5-3}$$

Table 5-1. System dependent variables for equation fitted to experimental data.

Variable	Low Pressure Side	High Pressure Side
A_1	2.5834904 m/s	3.5191821 m/s
A_2	$-A_4$	$-A_4$
A_3	300.59068 m/s	286.50994 m/s
A_4	$-A_2$	$-A_2$
A_5	639132.87 m/s	102031.60 m/s
A_6	-77601569 m/s	-5604354.6 m/s
α	0.66666667	0.66666667
β	-0.25000000	-0.25000000
δ	1.2500000	1.2500000
P_c	4.6081493 MPa	

Critical temperature

To begin the search for the critical temperature, the temperature and pressure can be sought which correspond to the minimum speed of sound for each individual data run. A plot of system temperature versus system pressure can be constructed to illustrate the dependence of the two system variables. Such a plot below the critical point would be a delineation of the coexistence curve between liquid and vapor states of a thermodynamic fluid. Above the critical point, such a plot would simply represent the line along which the system most closely approached the critical density. Figure

5-16 is a plot of system temperature versus system pressure where each individual point is at the minimum system speed of sound for an individual data run.

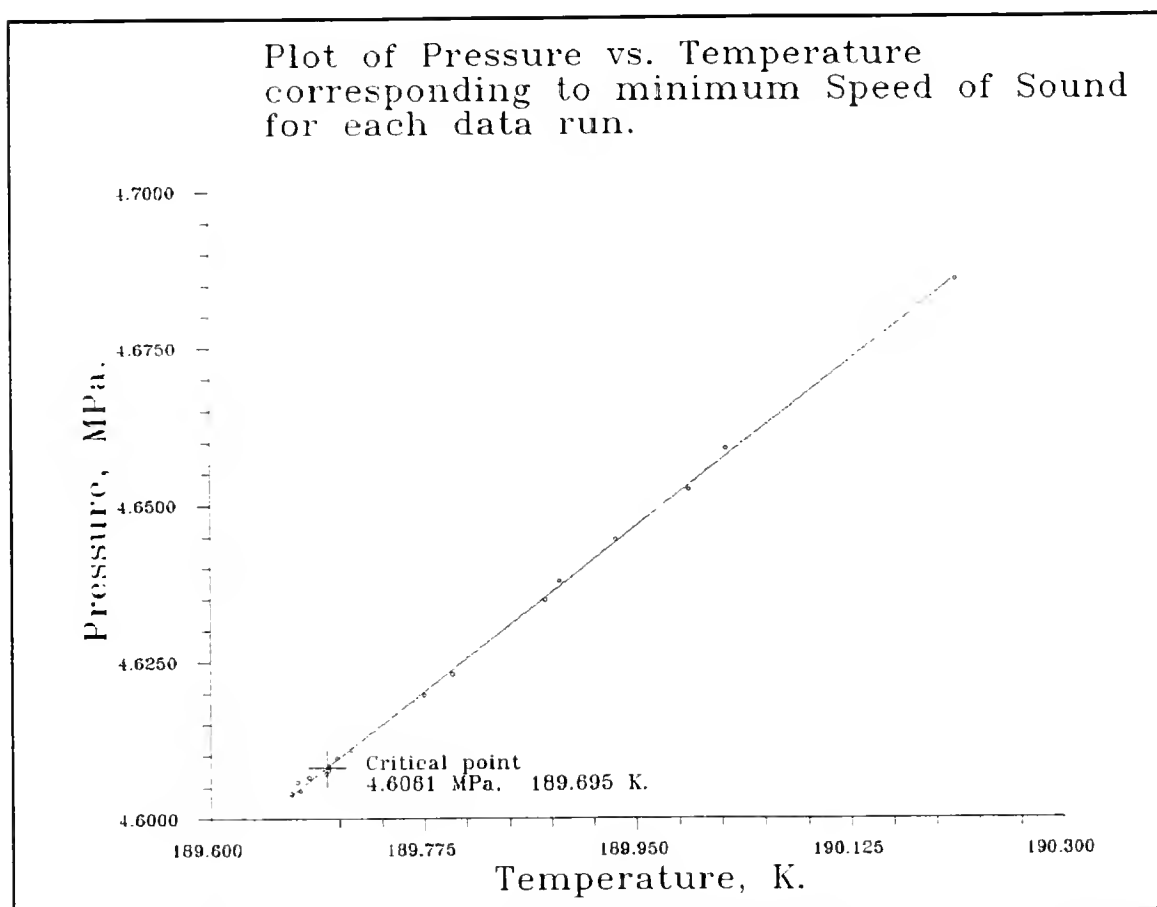


Figure 5-16. Plot of system temperature versus system pressure corresponding to minimum values for system speed of sound for each data run.

The line drawn in figure 5-16 is straight. However, the coexistence curve between liquid and vapor states for a thermodynamic fluid is not constrained to be straight at all. Still, any curve can be approximated by a straight line provided the arc length under scrutiny is held to a small

interval. The temperature value for the critical point lies somewhere along the line drawn in figure 5-16.

The value for the critical pressure found earlier can be substituted into the equation of the line shown in figure 5-16 and the critical temperature can be calculated directly. The equation of the line is $P = (0.150768\text{MPa/K})T - 23.9918\text{MPa}$. From this equation, the critical temperature is 189.695K.

Thermodynamic Surface

The existence of equations that model the experimental results in an analytical manner leads to the possibility of illustrating the thermodynamic surface at the critical point. Figure 5-17 is an extrapolation of the analytical equations up to, through and beyond the critical point of Methane.

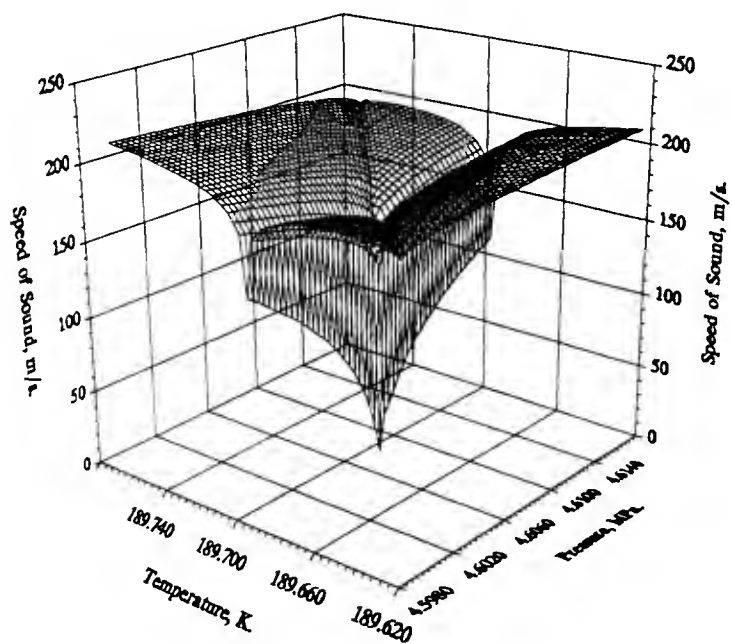


Figure 5-17. Thermodynamic surface of the critical point of methane.

CHAPTER 6 DISCUSSION

The Critical Point of Methane

The final critical values determined from this work are as follows...

$$P_c = 4.6081\text{MPa.} \pm .0015\text{MPa.}$$

$$T_c = 189.695\text{K} \pm .021\text{K}$$

Critical parameters gathered from work published in the past are listed in table 6-1 along with the present values to facilitate comparison. Scrutiny of the values in table 6-1 illustrates that this work will not lay to rest the controversy over the location of the critical point of methane. Ample precedence exists for a higher critical pressure than the latest value obtained by Kleinrahm and coworkers. However, there is no earlier indication that the value for the critical temperature should be as low as that found during the course of this work.

Such a situation leaves the author on the horns of a dilemma. It would be the height of hubris to claim offhand that this current piece of work is correct and all previous work incorrect. Lack of first hand experience with techniques utilized by previous researchers makes criticism of their work

Temperature	Pressure	Density	Researcher	year
190.50	4.6204	162.3	Cardoso, (45)	1915
190.75	4.6397	161.3	Keyes, (46)	1922
190.65	4.6306	n/a	Bennewitz & Andreeva,	1929
190.54	4.6072	162.5	Bloomer & Parrent,	1953
191.05	4.6306	n/a	Timrot & Pavlovitch,	1959
190.6	4.6204	162.6	Grigor & Steele, (50)	1968
190.58	n/a	166.0	Ricci & Scafe, (51)	1969
190.77*	4.6265	162.5	Vennix, et al., (52)	1970
190.53*	4.5947	162.8	Jansoone, et al., (53)	1970
190.50	4.595	163.0	Pope, et al., (54)	1973
190.55*	4.595	159.6	Gielen, et al., (55)	1973
190.564**	4.5922	162.66	Kleinrahm, et al.,	1986
189.695**	4.6081	n/a	This Work	1993
* Based on International Temperature Scale of 1968.				
** Based on International Temperature Scale of 1990.				

Table 6-1. Methane critical point parameters found in the literature.

difficult. It is possible, however, to look for potential systematic errors that might exist in this work. Once such a search is complete, the precision of this technique can be favorably demonstrated and a comparison of this data to that obtained from previous work can be made.

Gas Impurity

In the reference cited just previous to this work in table 6-1, the quality of the methane utilized by Kleinrahm and coworkers was stated as 99.9995% pure. The methane utilized for this work was only 99.99% pure. The addition of certain gases, most notably hydrogen or helium, could definitely affect the results of this experiment and yield inaccurate critical parameters. Both Hydrogen and Helium gas typically accompany natural gas in its native state. However, to identify the initial gas as the source of possibly inaccurate results is inadequate without some type of instrumental verification. Such verification was unavailable at the time of this experiments performance.

System RTD

The Keithley 196A DMM used to measure the resistance of the system RTD was purchased precalibrated from its manufacturer. The accompanying instruction manual directed that the DMM should be recalibrated once a year as a precaution to ensure instrument accuracy. Since the DMM had

been obtained less than six months previous to performance of this experiment, calibration was deemed unnecessary. Also, a precision resistor was required, but unavailable.

As a precaution, the Keithley 196A was checked against the precalibrated RTD. Resistance values corresponding to temperature values were supplied by the RTD's manufacturer. If the DMM was properly calibrated, it should always produce resistance values that matched resistance values supplied by the RTD manufacturer for a specific temperature. The precalibrated RTD was checked against the known temperature value for the triple point of water. The difference between the DMM resistance reading and the stated manufacturer's resistance value was treated as an offset throughout the experiment. The necessity of using a resistance offset to reconcile the DMM to actual temperature values might indicate that the DMM had further systematic errors that went undetected.

Finally, the physical location of the system RTD was above the spherical resonator. The flow of methane was into the bottom of the resonator and out the top. Placement of the system RTD as close to the point at which the methane was being examined by acoustic excitation was essential. However, the constant temperature environment was kept cool by utilization of liquid nitrogen which has a boiling point of 77K. The liquid nitrogen was introduced into a mixing chamber for evaporation and then into the constant temperature

environment directly through the blades of circulating fans. Potentially, the temperature directly adjacent to the circulating fans might have been colder than the rest of the environment. The fans were located near the top of the constant temperature environment on one side and near the bottom on the other side to provide maximum cross circulation. It is possible that the location of the system RTD near the top of the constant temperature environment might have been an error. A shield or physical barrier was placed between the circulating fans and the RTD shroud during all experiments to help alleviate this potential error, but it must be mentioned in order to be thorough.

Heise Pressure Gauge

The Heise pressure gauge was calibrated against an absolute dead weight pressure. However, calibration did not extend into the region of pressure necessary for this experiment. It was assumed that extrapolation of the pressure calibration to higher pressures was legitimate because of the extreme linearity of the calibration plot at lower pressures. Such an assumption may not have been appropriate. Still, great care was exercised in the calibration of the Heise pressure gauge as well as all of the measurement devices.

Precision of Technique

Figure 6-1 and 6-2 are excerpts of data presented earlier in this report. They illustrate data taken close to the critical density. Examination of the two graphs exhibits the precision of the current technique. In each, the uncertainty of where one line ends its descent and the other begins its ascent is limited to no more than 0.0015MPa or 0.22psi.

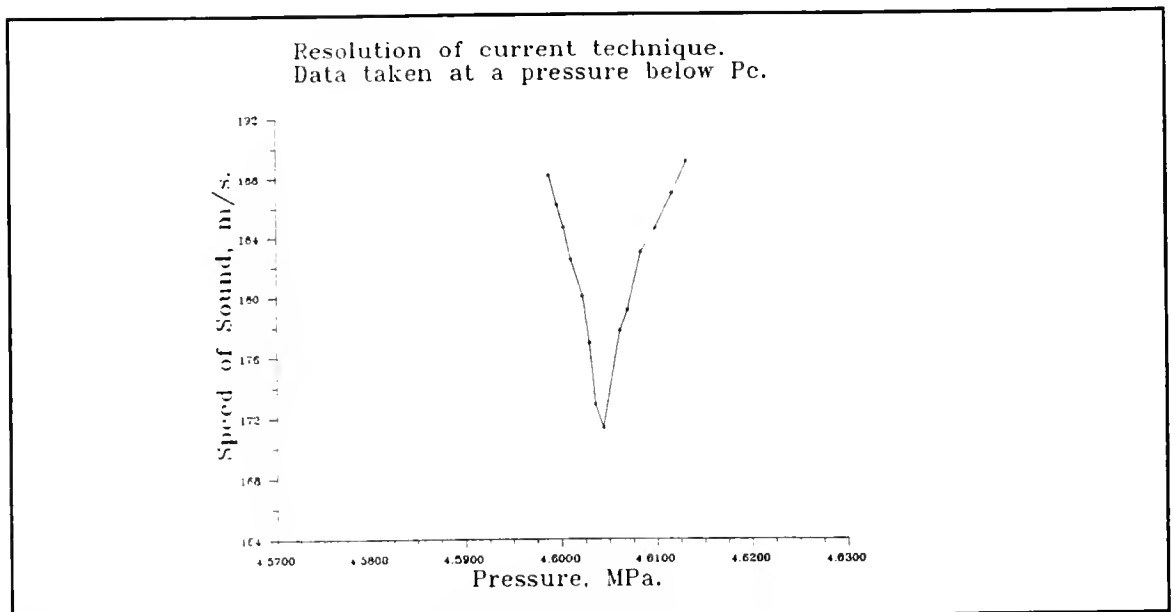


Figure 6-1. Sub critical pressure data taken near the critical density.

Figure 6-3 is a composite graph produced from three sources; data taken from an experiment by Gammon and Douslin⁵⁷, data taken from a report by Sivaraman and Gammon⁵⁸ and data generated from a theoretical model proposed by Jin, Tang and Sengers.⁵⁹ Actual data represented in figure 6-3

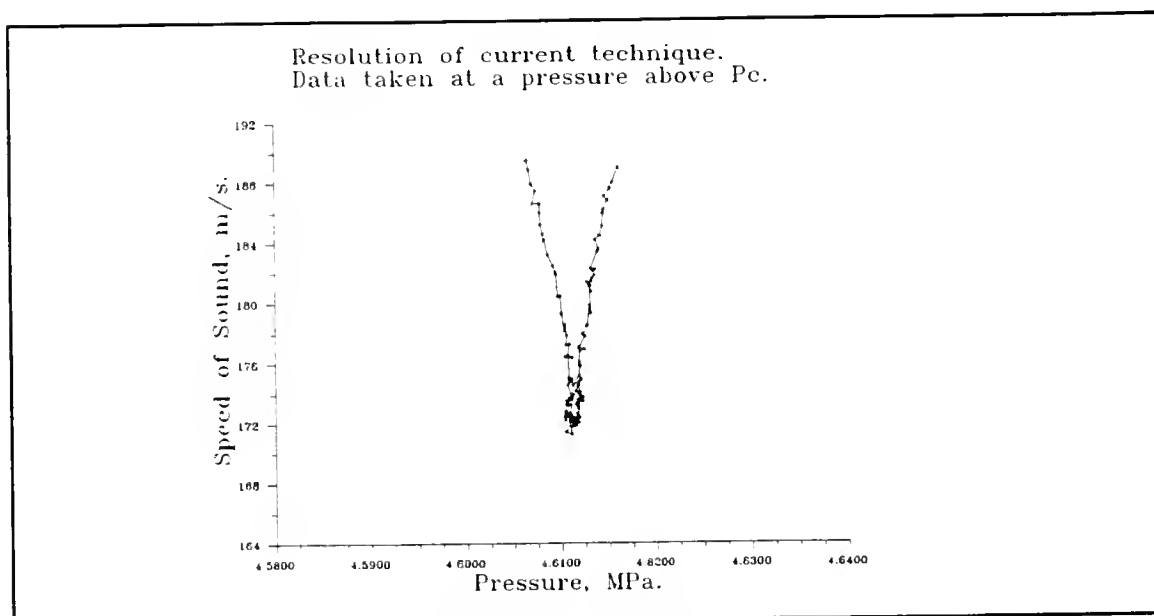


Figure 6-2. Above critical pressure data taken near the critical density.

was gained from an experiment which utilized an isochoric cylindrical resonator instead of an isothermal spherical resonator as in this work. Information represented in figure 6-1 was not intended to give a precise measurement of the critical point of methane. Rather, it was intended to illustrate the potential sensitivity of the technique as a probe for the critical point of any thermodynamic fluid.

Figure 6-4 is a graph of twenty data sets collected for this work plotted identically to the data contained in figure 6-3. It can be readily seen that the precision of the technique utilized for this report is extremely high. No other technique has been able to look at data as tightly clustered as the current work is capable of on a routine basis. Work done by researchers in this group in the past utilizing related sonic techniques has routinely been within

.01% of previously accepted literature values. Such excellent agreement has been attained for fluids that were much less demanding in terms of the ability to work at the temperature and pressure of their critical region.

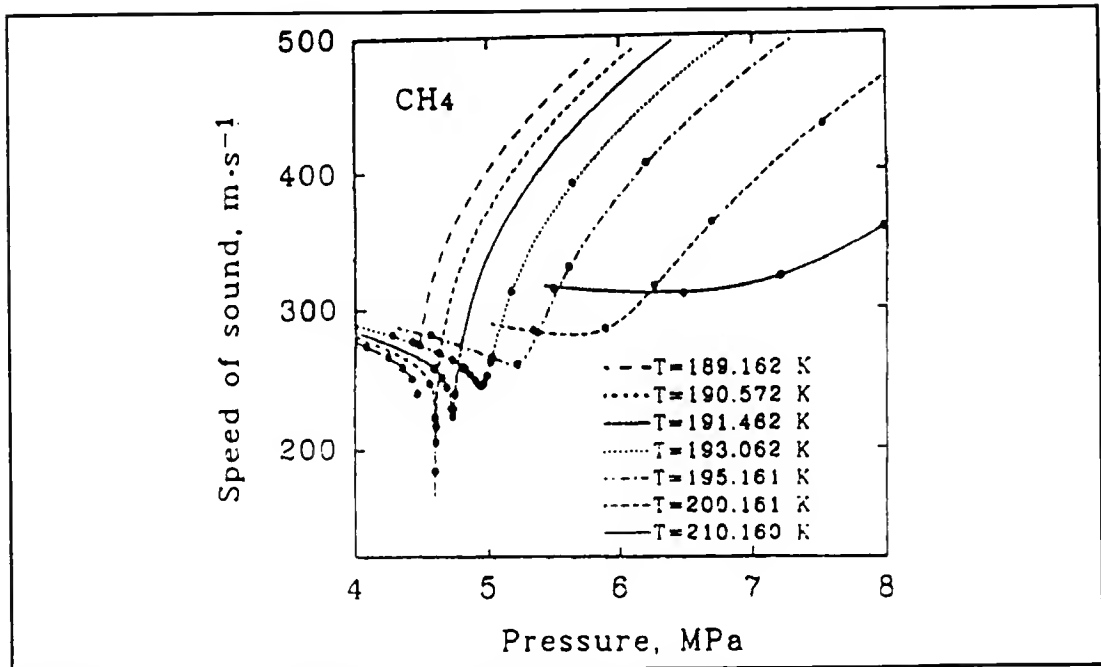


Figure 6-3. Sound velocity at selected temperatures as a function of pressure.

Personal Note

The initial pressure loading of the spherical resonator system with methane was followed on a Dynamic Signal Analyzer, (DSA). Once the system was loaded with the anticipated critical pressure, the DSA was used to check whether or not it was possible to find a minimum in the speed of sound of the system within the range of the bellows movement. The DSA was utilized because it was capable of performing a 12 bit fast

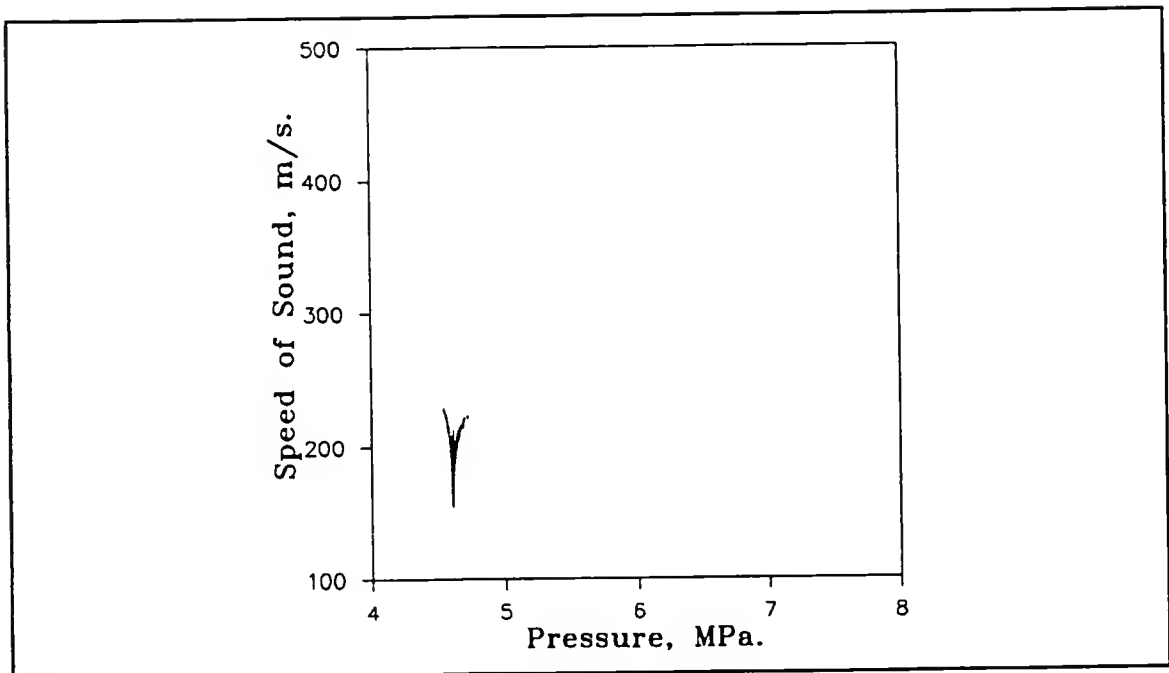


Figure 6-4. Graph of sound velocity as a function of pressure containing all twenty data runs from this experiment.

Fourier transform on acoustic data and displaying the resulting frequency data at 32 times a minute. Changes of conditions within the spherical resonator system could be followed very closely. If the spherical resonator system had insufficient or excess methane within it, the discrepancy could be discovered quite quickly and the system pressure could be adjusted accordingly.

As the overall system conditions approached very near the conditions that exist at the critical point of methane, frequency data displayed on the DSA became dampened and moved very rapidly toward zero frequency. Eventually, the system became too dynamic, and the DSA proved incapable of keeping pace with changing conditions. The decision was made to

switch to the more accurate method of following frequency data that the master data computer afforded; namely a 17 bit fast Fourier transform capability. Before the changeover, however, temperature was dropped steadily and volume was expanded steadily in an attempt to reach the critical point conditions. Frequency data dropped steadily until the anticipated critical point conditions were reached, but the frequency data continued to move to lower values even after this point.

It was assumed at the time that further tweaking of the system variables was required to zero in on the critical point conditions and that such adjustment could be made only after careful study of the more accurate methods employed by the master data computer algorithms. Temperature and volume changes were allowed to continue, however, in an attempt to find the point at which the frequency data would begin to move to higher values, (as has been observed in several graphs presented in previous chapters of this report). At a point approximately one degree lower and one psi higher than the anticipated critical point conditions, frequency response on the DSA moved rapidly toward zero and went completely flat at maximum signal amplification for a period of about ten seconds. When frequency response resumed, the frequency data did indeed move to higher values.

Since the temperature and pressure values were so far removed from the anticipated critical point values, the observed phenomenon was looked upon as being interesting, but

not necessarily as something more significant. Consequently, the temperature and pressure values that corresponded to the occurrence of the phenomena were only noted in passing and were not recorded in any detail. In retrospect, it is highly possible that experimental conditions had actually duplicated the critical point conditions for a few moments. The phenomenon being observed likely was the attainment or near attainment of zero speed of sound. Such an event has never been reported before in the literature. Such an event also raises the possibility of a new probe for the critical point of thermodynamic fluids; namely the pinpoint observation of zero frequency response corresponding to the critical point conditions. Routine ability for such an observation can be attained only through the use of more capable DSA's, but with the rapid change occurring in electronic instrumentation, such capability is likely to arise in the future.

REFERENCE LIST

1. Josten, Melvin D., Johnston, David O., Netterville, John T., Wood, James L., World of Chemistry, Saunders College Publishing, Philadelphia, Pa., 1991.
2. Atkins, P. W., Physical Chemistry, 3rd. ed., W. H. Freeman and Company, New York, New York, 1986.
3. Eliezer, Shalom, Ghatak, Ajoy L., Hora, Heinrich, An Introduction to Equations of State: Theory and Applications, Cambridge University Press, Cambridge, Great Britain, 1986.
4. R. Kleinrahm and W. Wagner, J. Chem. Thermodynam., 18:739, 1986.
5. Kurumov, D. S., Olchoway, G. A., Sengers, J. V., Int. J. Thermophys., 9:73, 1988.
6. Jin, G. X., Tang, S., Sengers, J. V., Int. J. Thermophys., 13:671, 1992.
7. Hirschfelder, Joseph O., Curtiss, Charles F., Bird, R. Byrom, Molecular Theory of Gases and Liquids, John Wiley and Sons, New York, New York, 1954.
8. Michels, A., Blaisse, B., Michels, C., Proc. Roy. Soc., London, A160, 358, 1937.
9. Ipatieff, V. N., Monroe, G. S., Ind. Eng. Chem., (Anal. Ed.), 14, 171, 1942.
10. Cagnaird de la Tour, Ann. Chim., (Ser. 2), 21, 127, 1922.
11. Cailletet, L., Mathias, E., Comptes Rendus de L'Academie Des Sciences, 102, 1202, 1886.
12. Cailletet, L., Mathias, E., Comptes Rendus de L'Academie Des Sciences, 104, 563, 1887.

13. Alberty, Robert A., Daniels, Farrington, Physical Chemistry, 5th ed., John Wiley & Sons, New York, 1979.
14. Bagatskii, M. I., Voronel', A. V., Guak, V. G., J. Exptl. Theoret. Phys. (USSR), 43, 728, 1962.
15. Voronel, A. V., Chashkin, Yu R., Popov, V. A., Simkin, V. G., J. Exptl. Theoret. Phys. (USSR), 45, 828, 1963.
16. Curtiss, C. F., Boyd, C. A., Palmer, H. B., J. Chem. Phys., 19, 801, 1951.
17. Kleinrahm, R., Wagner, W., J. Chem. Thermodynam., 18:739 1986.
18. Adamson, Arthur A., A Textbook of Physical Chemistry, 2nd Ed., Academic Press, New York, 1979.
19. Kinsler, Lawrence E. and Frey, Austin R., Fundamentals of Acoustics, 2nd Ed., John Wiley & Sons, Inc., New York, 1967.
20. Morse, Philip M. and Ingard, K. Uno, Theoretical Acoustics, McGraw-Hill, Inc, 1968.
21. Lord Rayleigh, Proc. London Math. Soc., 1, iv 93, 1872.
22. Ferris, Horace G., J. Acoust. Soc. Am., 24, 1, 57, 1952.
23. Mehl, James B. and Moldover, R., J. Chem. Phys., 74, 7, 4062, 1981.
24. Mehl, James B., J. Acoust. Soc. Am., 71, 5, 1109, 1982.
25. McGlashan, M. L., J. Chem. Thermodynamics, 22, 653-663, 1990.
26. Shoemaker, David P., Garland, Carl W., Nibler, Joseph W., Experiments in Physical Chemistry, 5th. ed., McGraw Hill Publishing Company, 1989.
27. Dejsupa, Chadin, Acoustic Determination of Phase Boundaries and Critical Points of Gases: CO₂, CO₂-C₂H₆ Mixture, and C₂H₆., Ph. D. Dissertation, The University of Florida, 1991.

28. Morse, Philip M., Ingard, K. Uno, Theoretical Acoustics, McGraw-Hill Book Company, NewYork, 1968.
29. Sona, C. F., An Acoustic Study of Gas and Vapors, Ph. D. Dissertation, The University of Florida, 1986.
30. Colgate, S. O., Sivaraman, A., Reed, K., Acoustic Determination of the Thermodynamic Reference State Heat Capacity of n-Heptane Vapor, Research Report RR-109, Project 831-83 through 86, Gas Processors Association, Tulsa Oklahoma, 1987.
31. Colgate, S. O., Sivaraman, A., Reed, K., Reference State Heat Capacities of Three C-8 Compounds, Research Report RR-123, Project 831, Gas Processors Association, Tulsa Oklahoma, 1989.
32. Reed, Kyle, Thermophysical Properties of Hydrocarbons Determined Using a Spherical Resonator, M.S. Thesis, The University of Florida, 1990.
33. Colgate, S. O., Sona, C. F., Reed, K. R., Sivaraman, A., J. Chem. Eng. Data, 35, 1, 1990.
34. Colgate, S. O., Sivaraman, A., Reed, K. R., J. Chem. Thermodynamics, 22, 245, 1990.
35. Colgate S. O., Sivaraman, A., Reed, K. R., Fluid Phase Equilibria, 60, 191, 1990.
36. Colgate, S. O., Sivaraman, A., Dejsupa, C., McGill, K. C., J. Chem. Thermodynamics, 23, 647, 1991.
37. Colgate, S. O., Sivaraman, A., Dejsupa, C., Fluid Phase Equilibria, 76, 175, 1992.
38. Colgate, S. O., Sivaraman, A., Dejsupa, C., Fluid Phase Equilibria, 79, 221, 1992.
39. Adamson, Arthur W., A Textbook of Physical Chemistry, 2nd. ed., Academic Press, New York, 1979.
40. Stell, G. R., Torquoto, S., Ind. Eng. Chem. Fundam., 17, 202, 1982.
41. Sivaraman, A., Magee, J. W., Kobayashi, R., Fluid Phase Equilibria, 16, 1, 1984.

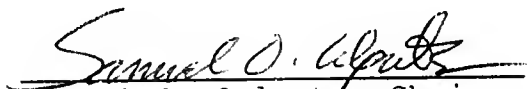
42. Sivaraman, A., Kragas, T., Kobayashi, R., Fluid Phase Equilibria, 16, 275, 1984.
43. Wegner, F. J., Phys. Rev. B, 5, 4529, 1972.
44. Ley-Koo, M., Green, M. S., Phys. Rev. A, 16, 2483, 1977.
45. Cardoso, E., J. Chim. Phys., v. 13, 1915.
46. Keyes, F. G., Smith, L. B., Joubert, D. B., J. Math. Phys. (M. I. T.), v.1, no. 4, 1922.
47. Bennewitz, K., Andreeva, N., Z. Physik. Chem., v. A142, 1929.
48. Bloomer, O. T., Parrent, J. D., Chem. Eng. Progress., Symp. Series., v. 49, 1952.
49. Timrot, D. L., Pavlovich, N. V., Nauchnyye doklady vysshey shkoly. Energetika, 1959.
50. Grigor, A. F., Steele, W. A., Experimental J. Chem. Phys., v. 48, 1968.
51. Ricci, F. P., Scafe, E., Phys. Letters, v. 29a, no. 11, 1969.
52. Vennix, A. J., Leland, T. W., Kobayashi, R., J. Chem. Eng. Data, v. 15, no. 2, 1970.
53. Jansoone, V., Gielen, H., Boelpaep, J. de, Verbeke, O. B., Physica, v. 46, no. 2, 1970.
54. Pope, G. A., Chappellear, P. S., Kobatashi, R., J. Chem. Phys., v. 59, no. 1, 1973.
55. Gielen, H., Jansoone, V., Verbeke, O. B., J. Chem. Phys., v. 59, no. 11, 1973.
56. Kleinrahm, R., Wagner, W., J. Chem. Thermodynam., 18:1109 1986.
57. Gammon, B. E., Douslin, D. R., J. Chem. Phys., 64, 203, 1976.
58. Sivaraman, A., Gammon, B. E., Speed- of Sound measurements in Natural Gas Fluids, Gas Research Institute Report 86/0043, Gas Research Institute, Chicago, Il., 1986.

59. Jin, G. X., Tang, S., Sengers, J. V., Int. J. Thermophys., 13, 4, july, 1992.

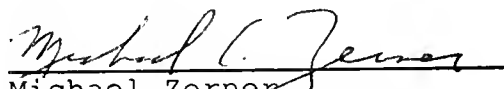
BIOGRAPHICAL SKETCH

The author, David Casey Rentz, was born August 6th, 1957. His parents are Raymond and Marilyn Rentz. His siblings are Laurie, Eric, Kevin and Erin. He married Ashley Elizabeth Light in May of 1992. He earned a Bachelor of Science degree from the University of Northern Iowa in 1983. He completed his graduate studies at the University of Florida in April of 1994.

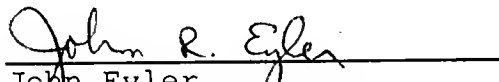
I certify that I have read this study and that in my opinion it conforms to acceptable standards of scholarly presentation and is fully adequate, in scope and quality, as a dissertation for the degree of Doctor of Philosophy.


Samuel O. Colgate, Chair
Associate Professor of Chemistry


I certify that I have read this study and that in my opinion it conforms to acceptable standards of scholarly presentation and is fully adequate, in scope and quality, as a dissertation for the degree of Doctor of Philosophy.


Michael Zerner
Professor of Chemistry


I certify that I have read this study and that in my opinion it conforms to acceptable standards of scholarly presentation and is fully adequate, in scope and quality, as a dissertation for the degree of Doctor of Philosophy.


John Eyler
Professor of Chemistry

I certify that I have read this study and that in my opinion it conforms to acceptable standards of scholarly presentation and is fully adequate, in scope and quality, as a dissertation for the degree of Doctor of Philosophy.


Robert Harvahan
Professor of Chemistry

I certify that I have read this study and that in my opinion it conforms to acceptable standards of scholarly presentation and is fully adequate, in scope and quality, as a dissertation for the degree of Doctor of Philosophy.


Zoran Pop-Stojanovic
Professor of Mathematics

This dissertation was submitted to the Graduate Faculty of the Department of Chemistry in the College of Liberal Arts and Sciences and was accepted as partial fulfillment of the requirements for the degree of Doctor of Philosophy.

April, 1994

Dean, Graduate School

LD
1780
1994
. R422 -

